MRTD: New Time-Domain Schemes Based on Multiresolution Analysis

Michael Krumpholz and Linda P. B. Katehi, *Fellow, IEEE*

Abstract— **The application of multiresolution analysis to Maxwell's equations results in new multiresolution time-domain (MRTD) schemes with unparalleled inherent properties. In particular, the approach allows the development of MRTD schemes which are based on scaling functions only or on a combination of scaling functions and wavelets leading to a variable mesh grading. The dispersion of the MRTD schemes compared to the conventional Yee finite-difference time-domain (FDTD) scheme shows an excellent capability to approximate the exact solution with negligible error for sampling rates approaching the Nyquist limit. Simple microwave structures including dielectric materials are analyzed in order to illustrate the application of the MRTD schemes and to demonstrate the advantages over Yee's FDTD scheme with respect to memory requirements and execution time.**

I. Introduction

THE finite difference time-domain (FDTD) method has proven to be a powerful numerical technique in electromagnetic field computation [1], [2]. Despite its simplicity and modeling versality, however, the technique suffers from serious limitations due to the substantial computer resources required to model electromagnetic problems with medium or large computational volumes. These limitations have always made it a matter of great interest to improve the efficiency of Yee's FDTD scheme and have led researchers to the development of various hybrid FDTD techniques [3], [4] and higher-order FDTD schemes [5], [6]. This paper is not about improving the efficiency of conventional FDTD, but about new time-domain schemes with highly linear dispersion characteristics resulting in significant reductions of computer resources.

The method of moments [7] provides a mathematically correct approach for the discretization of integral and partial differential equations. The application of the method of moments for the discretization of Maxwell's equations has lead to the field theoretical foundation of the TLM method [8], [9]. In addition, it has been shown in [8] and [10] that Yee's FDTD scheme can be derived using the same approach with pulse functions for the expansion of the unknown fields. Since the method of moments allows for the use of any complete set of orthonormal basis functions, the use of an appropriate set may lead to new time-domain and frequency domain schemes. In literature [11], [12], the use of scaling and wavelet functions as a complete set of basis functions is called multiresolution analysis. In this paper we show that the application of multiresolution analysis in the method of moments for the discretization of Maxwell's equations leads to new multiresolution time-domain (MRTD) schemes.

For the derivation of the MRTD schemes, the electromagnetic fields are represented by a two-fold expansion in scaling and wavelet functions with respect to space. The expansion in terms of scaling functions only leads to the S-MRTD scheme which allows for a correct modeling of smoothly-varying electromagnetic fields. In regions characterized by strong field variations or field singularities, additional field sampling points are introduced by incorporating wavelets in the field expansions. MRTD schemes based on both scaling and wavelet functions are denoted throughout this paper by W-MRTD schemes. In order to obtain two-step MRTD schemes with respect to time, pulse functions are used as expansion and test functions in time domain.

The S-MRTD and W-MRTD schemes are derived using cubic spline Battle–Lemarie scaling and wavelet functions [13], [14]. This orthonormal wavelet expansion has already been applied successfully for the computation of electromagnetic field problems in frequency domain [15], [16]. The Battle–Lemarie scaling and wavelet functions do not have compact support, thus the MRTD schemes have to be truncated with respect to space. However, this disadvantage is offset by the low-pass and band-pass characteristics in spectral domain, allowing for an *a priori* estimate of the number of resolution levels necessary for a correct field modeling. Furthermore, for this type of scaling and wavelet functions, the evaluation of the moment method integrals is simplified due to the existence of closed form expressions in spectral domain and simple representations in terms of cubic spline functions in space domain.

The use of nonlocalized basis functions cannot accomodate localized boundary conditions and cannot allow for a localized modeling of the material properties. To overcome this difficulty, the image principle is used to model perfect electric and magnetic boundary conditions. As for the description of material parameters, the constitutive relations are discretized accordingly so that the relationships between the electric/magnetic flux and the electric/magnetic field are given by matrix equations. A complete dispersion analysis of the S-MRTD and W-MRTD schemes including a comparison to Yee's FDTD scheme is given and shows the superiority of the

Manuscript received June 10, 1995; revised December 18, 1995. This work was supported in part by a scholarship of the NATO Science Committee through the German Academic Exchange Service and by the U.S. Army Research Office.

The authors are with the Radiation Laboratory, Department of Electrical Engineering and Computer Science, University of Michigan, Ann Arbor, MI 48109-2122 USA.

Publisher Item Identifier S 0018-9480(96)02346-0.

MRTD method to all other existing discretization techniques. Specifically, the results show the capability of MRTD to provide excellent accuracy with up to two discretization points per wavelength only, representing the Nyquist sampling limit.

II. The S-MRTD Scheme

At first, for simplicity, we will derive the S-MRTD scheme for a homogeneous medium. The derivation is similar to that of Yee's FDTD scheme which uses the method of moments with pulse functions as expansion and test functions [10]. For the derivation of S-MRTD, the field components are represented by a series of scaling functions in space and and pulse functions in time. Furthermore, as for Yee's FDTD scheme, the field expansions of the magnetic field components are shifted by half a discretization interval in space and time with respect to the field expansions of the electric field components.

A. Derivation of the S-MRTD Scheme

Maxwell's first vector equation

$$\nabla \times \boldsymbol{H} = \varepsilon \frac{\partial \boldsymbol{E}}{\partial t} \tag{1}$$

for a homogeneous medium with the permittivity ε may be written in the form of three scalar cartesian equations as

$$\frac{\partial H_z}{\partial y} - \frac{\partial H_y}{\partial z} = \varepsilon \frac{\partial E_x}{\partial t} \tag{2}$$

$$\frac{\partial H_x}{\partial z} - \frac{\partial H_z}{\partial x} = \varepsilon \frac{\partial E_y}{\partial t} \tag{3}$$

$$\frac{\partial H_y}{\partial x} - \frac{\partial H_x}{\partial y} = \varepsilon \frac{\partial E_z}{\partial t}. \tag{4}$$

In the same way, the second Maxwell's vector equation for a homogeneous medium with the permeability μ

$$\nabla \times \boldsymbol{E} = -\mu \frac{\partial \boldsymbol{H}}{\partial t} \tag{5}$$

can be split into three scalar equations similar to (2), (3) and (4). The electric and magnetic field components incorporated in these equations are expanded as following

$$E_x(\vec{r},t) = \sum_{k,l,m,n,=-\infty}^{+\infty} {}_kE^{\phi x}_{l+1/2,m,n} h_k(t)\phi_{l+1/2}(x) \cdot \phi_m(y)\phi_n(z)$$

$$E_y(\vec{r},t) = \sum_{k,l,m,n,=-\infty}^{+\infty} {}_kE^{\phi y}_{l,m+1/2,n} h_k(t)\phi_l(x) \cdot \phi_{m+1/2}(y)\phi_n(z)$$

$$E_z(\vec{r},t) = \sum_{k,l,m,n,=-\infty}^{+\infty} {}_kE^{\phi z}_{l,m,n+1/2} h_k(t)\phi_l(x) \cdot \phi_m(y)\phi_{n+1/2}(z)$$

$$H_x(\vec{r},t) = \sum_{k,l,m,n=-\infty}^{+\infty} {}_{k+1/2}H^{\phi x}_{l,m+1/2,n+1/2} h_{k+1/2}(t) \cdot \phi_l(x)\phi_{m+1/2}(y)\phi_{n+1/2}(z)$$

$$H_y(\vec{r},t) = \sum_{k,l,m,n=-\infty}^{+\infty} {}_{k+1/2}H^{\phi y}_{l+1/2,m,n+1/2} h_{k+1/2}(t) \cdot \phi_{l+1/2}(x)\phi_m(y)\phi_{n+1/2}(z)$$

$$H_z(\vec{r},t) = \sum_{k,l,m,n=-\infty}^{+\infty} {}_{k+1/2}H^{\phi z}_{l+1/2,m+1/2,n} h_{k+1/2}(t) \cdot \phi_{l+1/2}(x)\phi_{m+1/2}(y)\phi_n(z) \tag{6}$$

where ${}_kE^{\phi\kappa}_{l,m,n}$ and ${}_kH^{\phi\kappa}_{l,m,n}$ with $\kappa = x, y, z$ are the coefficients for the field expansions in terms of scaling functions. The indexes l, m, n, and k are the discrete space and time indices related to the space and time coordinates via $x = l\Delta x, y = m\Delta y, z = n\Delta z$ and $t = k\Delta t$, where $\Delta x, \Delta y, \Delta z$ and Δt represent the space and time discretization intervals in x-, y-, z- and t-direction. The function $h_m(x)$ is defined as

$$h_m(x) = h\left(\frac{x}{\Delta x} - m\right) \tag{7}$$

with the rectangular pulse function

$$h(x) = \begin{cases} 1 & \text{for } |x| < 1/2 \\ 1/2 & \text{for } |x| = 1/2 \\ 0 & \text{for } |x| > 1/2 \end{cases}. \tag{8}$$

The function $\phi_m(x)$ is defined as

$$\phi_m(x) = \phi\left(\frac{x}{\Delta x} - m\right) \tag{9}$$

where $\phi(x)$ represents the cubic spline Battle–Lemarie scaling function [13], [14] depicted in Fig. 1. Assuming the Fourier transformation

$$\tilde{\phi}(\lambda) = \int_{-\infty}^{+\infty} \phi(x) e^{j\lambda x}\, dx \tag{10}$$

and

$$\phi(x) = \frac{1}{2\pi} \int_{-\infty}^{+\infty} \tilde{\phi}(\lambda) e^{-j\lambda x}\, d\lambda \tag{11}$$

respectively, the closed-form expression of the scaling function in spectral domain is given by [17]

$$\tilde{\phi}(\lambda) = \left(\frac{\sin\left(\frac{\lambda}{2}\right)}{\frac{\lambda}{2}} \right)^4 \cdot \frac{1}{\sqrt{1 - \frac{4}{3}\sin^2\left(\frac{\lambda}{2}\right) + \frac{2}{5}\sin^4\left(\frac{\lambda}{2}\right) - \frac{4}{315}\sin^2\left(\frac{\lambda}{2}\right)}} \tag{12}$$

with the low-pass spectral domain characteristics shown in Fig. 2.

We insert the field expansions in Maxwell's equations and sample the equations using pulse functions as test functions in time and scaling functions as test functions in space. For the sampling with respect to time, we need the following integrals [10]

$$\int_{-\infty}^{+\infty} h_m(x) h_{m'}(x)\, dx = \delta_{m,m'} \Delta x \tag{13}$$

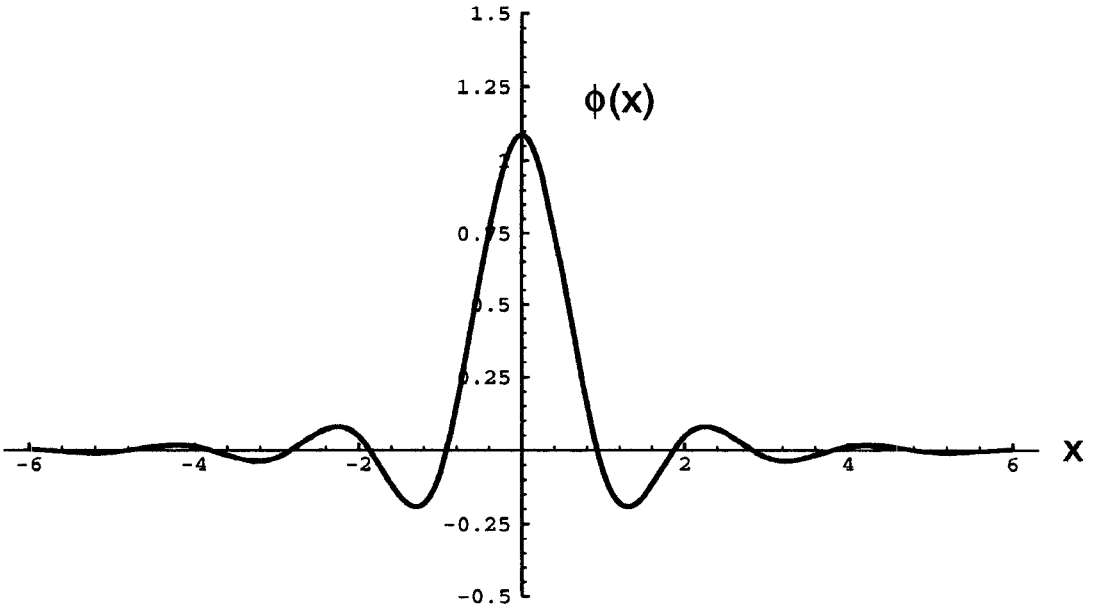

Fig. 1. Cubic spline Battle–Lemarie scaling function in space domain.

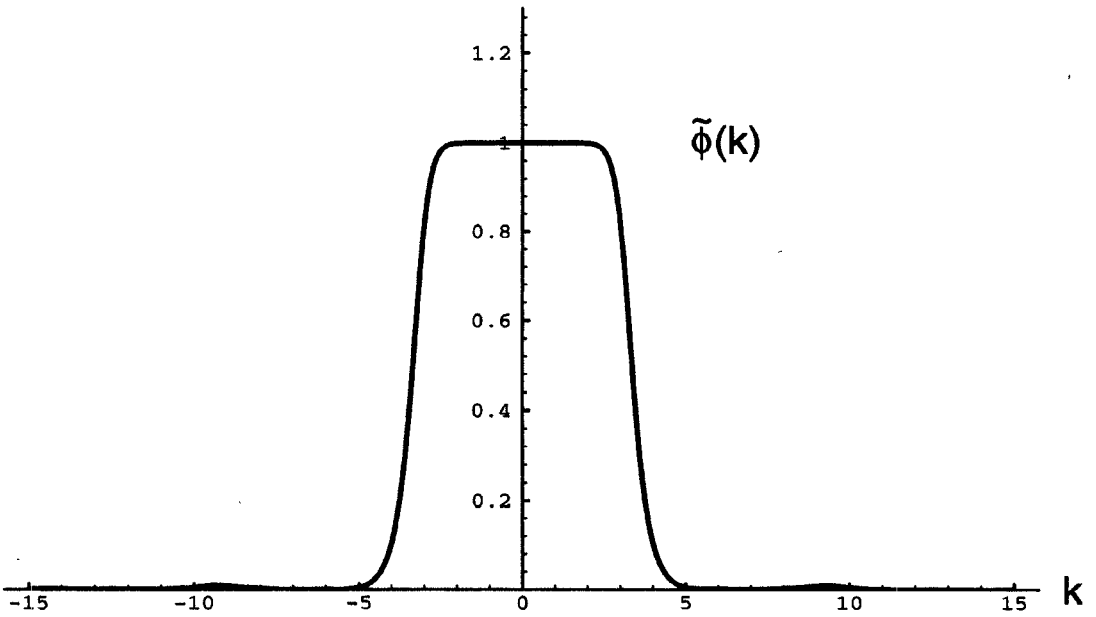

Fig. 2. Cubic spline Battle–Lemarie scaling function in spectral domain.

where $\delta_{m,m'}$ represents the kronecker symbol

$$\delta_{m,m'} = \begin{cases} 1 & \text{for } m = m' \\ 0 & \text{for } m \neq m' \end{cases} \tag{14}$$

and

$$\int_{-\infty}^{+\infty} h_m(x) \frac{\partial h_{m'+1/2}(x)}{\partial x}\, dx = \delta_{m,m'} - \delta_{m,m'+1}. \tag{15}$$

For the sampling with respect to space, we use the orthogonality relation for the scaling functions [17]

$$\int_{-\infty}^{+\infty} \phi_m(x)\phi_{m'}(x)\, dx = \delta_{m,m'}\Delta x. \tag{16}$$

To calculate the integral corresponding to (15) for scaling functions, we make use of the closed form expression of the scaling function in spectral domain. According to Galerkin's method [7], for complex basis functions, one has to choose the complex conjugant of the basis functions as test functions. We then obtain

$$\int_{-\infty}^{+\infty} \phi_m(x) \frac{\partial \phi_{m'+1/2}(x)}{\partial x}\, dx = \frac{1}{\pi}\int_0^{\infty} |\tilde{\phi}(\lambda)|^2 \lambda \sin \lambda(m' - m + 1/2)\, d\lambda \tag{17}$$

where $\tilde{\phi}(\lambda)$ is given by (12). This integral may be evaluated

TABLE I
THE COEFFICIENTS $a(i)$

i	$a(i)$
0	1.2918462
1	-0.1560761
2	0.0596391
3	-0.0293099
4	0.0153716
5	-0.0081892
6	0.0043788
7	-0.0023433
8	0.0012542

numerically resulting in

$$\int_{-\infty}^{+\infty} \phi_m(x) \frac{\partial \phi_{m'+1/2}(x)}{\partial x}\, dx = \sum_{\imath=-\infty}^{+\infty} a(i)\delta_{m+\imath,m'}. \quad (18)$$

The coefficients $a(i)$ for $0 \le i \le 8$ are shown in Table I, and the coefficients $a(i)$ for $i<0$ are given by the symmetry relation $a(-1-i) = -a(i)$. The Battle–Lemarie scaling function does not have compact but only exponential decaying support and thus, the coefficients $a(i)$ for $i>8$ are not zero. However, we found that these coefficients are negligible, affecting the accuracy of the field computation only for very low values of the wave vector. We therefore use the approximation

$$\int_{-\infty}^{+\infty} \phi_m(x) \frac{\partial \phi_{m'+1/2}(x)}{\partial x}\, dx \approx \sum_{\imath=-9}^{+8} a(i)\delta_{m+\imath,m'} \quad (19)$$

in order to obtain a MRTD scheme useful for practical applications.

As an example, we consider the discretization of (2). Sampling the term on the right-hand side of this equation, $\partial E_x/\partial t$, in space and time yields

$$\begin{aligned}
&\iiiint \frac{\partial E_x}{\partial t}\phi_{l+1/2}(x)\phi_m(y)\phi_n(z)h_{k+1/2}(t)\, dx\, dy\, dz\, dt \\
&\quad = \sum_{k',l',m',n'=-\infty}^{+\infty} {}_{k'}E^{\phi z}_{l'+1/2,m',n'}\delta_{l,l'}\delta_{m,m'}\delta_{n,n'} \\
&\qquad \cdot (\delta_{k+1,k'} - \delta_{k,k'})\Delta x\Delta y\Delta z \\
&\quad = ({}_{k+1}E^{\phi z}_{l+1/2,m,n} - {}_{k}E^{\phi z}_{l+1/2,m,n})\Delta x\Delta y\Delta x. \quad (20)
\end{aligned}$$

Sampling the first term on the left-hand side, $\partial H_z/\partial y$, in space and time using the same test functions yields

$$\begin{aligned}
&\iiiint \frac{\partial H_z}{\partial y}\phi_{l+1/2}(x)\phi_m(y)\phi_n(z)h_{k+1/2}(t)\, dx\, dy\, dz\, dt \\
&\quad = \sum_{k',l',m',n'=-\infty}^{+\infty} {}_{k'+1/2}H^{\phi z}_{l'+1/2,m'+1/2,n'}\delta_{l,l'}\delta_{n,n'}\delta_{k,k'} \\
&\qquad \cdot \left(\sum_{\imath=-9}^{+8} a(i)\delta_{m+i,m'}\right)\Delta x\Delta z\Delta t \\
&\quad = \left(\sum_{\imath=-9}^{+8} a(i)_{k+1/2}H^{\phi z}_{l+1/2,m+\imath+1/2,n}\right)\Delta x\Delta z\Delta t. \quad (21)
\end{aligned}$$

Proceeding in the same way with the term $\partial H_y/\partial z$, we obtain a difference equation for a homogeneous medium with the permittivity ε

$$\begin{aligned}
&\frac{\varepsilon}{\Delta t}({}_{k+1}E^{\phi x}_{l+1/2,m,n} - {}_{k}E^{\phi x}_{l+1/2,m,n}) \\
&\quad = \frac{1}{\Delta y}\sum_{\imath=-9}^{+8} a(i)_{k+1/2}H^{\phi z}_{l+1/2,m+\imath+1/2,n} \\
&\qquad - \frac{1}{\Delta z}\sum_{i=-9}^{+8} a(i)_{k+1/2}H^{\phi y}_{l+1/2,m,n+\imath+1/2}. \quad (22)
\end{aligned}$$

In order to provide a more compact form of this equation, we use the state-space representation for the electromagnetic field which was originally developed for the TLM method by Russer *et al.* [18]. We introduce the product space

$$\mathcal{H}_{m\otimes t} = \mathcal{H}_m \otimes \mathcal{H}_t \quad (23)$$

and define the electric and magnetic field component vectors $|E_{\phi\kappa}\rangle$ and $|H_{\phi\kappa}\rangle$ with $\kappa = x, y, z$ as vectors in $\mathcal{H}_{m\otimes t}$

$$|E_{\phi\kappa}\rangle = \sum_{k,l,m,n=-\infty}^{+\infty} {}_{k}E^{\phi\kappa}_{l,m,n}|k;l,m,n\rangle \quad (24)$$

and

$$|H_{\phi\kappa}\rangle = \sum_{k,l,m,n=-\infty}^{+\infty} {}_{k}H^{\phi\kappa}_{l,m,n}|k;l,m,n\rangle. \quad (25)$$

The orthonormal basis vectors of $\mathcal{H}_{m\otimes t}$ are given by the ket-vectors

$$|k;l,m,n\rangle = |k\rangle \otimes |l,m,n\rangle. \quad (26)$$

The vectors $|l,m,n\rangle$ represent a system of orthonormal basis vectors in the Hilbert space $\mathcal{H}_m$, where each node with the discrete coordinates (l,m,n) is assigned a basis vector $|l,m,n\rangle$. In the Hilbert space $\mathcal{H}_t$, the basis vector $|k\rangle$ corresponds to the discrete-time coordinate k. Due to the summation of k,l,m and n, the electric field component vector $|E_{\phi\kappa}\rangle$ combines all electric field components ${}_{k}E^{\phi\kappa}_{l,m,n}$ of the complete mesh at all discrete-time points k. The same is true for the magnetic field component vector $|H_{\phi\kappa}\rangle$. Thus the complete time evolution of a field component in four-dimensional space-time may be represented by a single vector in $\mathcal{H}_{m\otimes t}$.

The bra-vector $\langle k;l,m,n|$ is the Hermitian conjugate of $|k;l,m,n\rangle$. The orthogonality relations are given by

$$\langle k_1;l_1,m_1,n_1|k_2;l_2,m_2,n_2\rangle = \delta_{k_1,k_2}\delta_{l_1,l_2}\delta_{m_1,m_2}\delta_{n_1,n_2}. \quad (27)$$

To describe a shift of the field components in space and time, we define the half shift operators $\boldsymbol{X}_h$ and its Hermitian conjugate $\boldsymbol{X}_h^\dagger$ by

$$\begin{aligned}
\boldsymbol{X}_h|k;l,m,n\rangle &= |k;l+1/2,m,n\rangle \\
\boldsymbol{X}_h^\dagger|k;l,m,n\rangle &= |k;l-1/2,m,n\rangle \equiv \boldsymbol{X}_h^{-1}|k;l,m,n\rangle \quad (28)
\end{aligned}$$

and the shift operators $\boldsymbol{X}$ and its Hermitian conjugate $\boldsymbol{X}^\dagger$ by

$$\begin{aligned}
\boldsymbol{X}|k;l,m,n\rangle &= |k;l+1,m,n\rangle \\
\boldsymbol{X}^\dagger|k;l,m,n\rangle &= |k;l-1,m,n\rangle \equiv \boldsymbol{X}^{-1}|k;l,m,n\rangle. \quad (29)
\end{aligned}$$

In the same way, we define the half shift operators $\boldsymbol{Y}_h$ and $\boldsymbol{Z}_h$ and the shift operators $\boldsymbol{Y}$ and $\boldsymbol{Z}$ for the spatial coordinates m and n, the half time shift operator $\boldsymbol{T}_h$ for the time coordinate k as well as their Hermitian conjugates.

Using the state-space representation, (22) may be represented by the operator equation

$$\varepsilon \boldsymbol{X}_h^\dagger \boldsymbol{T}_h^\dagger \boldsymbol{d}_t |E_{\phi x}\rangle = \boldsymbol{X}_h^\dagger \boldsymbol{T}_h^\dagger (\boldsymbol{D}_Y^\phi |H_{\phi z}\rangle - \boldsymbol{D}_Z^\phi |H_{\phi y}\rangle) \tag{30}$$

where the difference operators $\boldsymbol{d}_t, \boldsymbol{D}_y^\phi$ and $\boldsymbol{D}_z^\phi$ are defined as

$$\boldsymbol{d}_t = \frac{1}{\Delta t}(\boldsymbol{T}_h^\dagger - \boldsymbol{T}_h) \tag{31}$$

and

$$\boldsymbol{D}_y^\phi = \frac{1}{\Delta y}\boldsymbol{Y}_h^\dagger \sum_{i=-9}^{+8} a(i)\boldsymbol{Y}^{-i}$$

$$\boldsymbol{D}_z^\phi = \frac{1}{\Delta z}\boldsymbol{Z}_h^\dagger \sum_{i=-9}^{+8} a(i)\boldsymbol{Z}^{-i}. \tag{32}$$

Proceeding in the same way with the five remaining scalar cartesian Maxwell's equations, we obtain five difference equations. By introducing the field vector

$$|F_\phi\rangle = \begin{bmatrix} |E_{\phi x}\rangle \\ |E_{\phi y}\rangle \\ |E_{\phi z}\rangle \\ |H_{\phi x}\rangle \\ |H_{\phi y}\rangle \\ |H_{\phi z}\rangle \end{bmatrix} \tag{33}$$

as a vector in the field state-space $\mathcal{H}_F$ [10]

$$\mathcal{H}_F = \mathcal{C}^6 \otimes \mathcal{H}_m \otimes \mathcal{H}_t \tag{34}$$

where $\mathcal{C}^6$ represents a six-dimensional complex vector space, the six difference equations may be represented by the operator equation

$$\boldsymbol{M}|F_\phi\rangle = 0 \tag{35}$$

where the operator $\boldsymbol{M}$ is given by (36), as shown at the bottom of the page, where the operator $\boldsymbol{D}_x^\phi$ is defined in a similar way as the operators $\boldsymbol{D}_y^\phi$ and $\boldsymbol{D}_z^\phi$.

The unit cell of the S-MRTD scheme, see Fig. 3, is similar to the unit cell of Yee's FDTD scheme. However, due to the different field expansions, the field components in the two schemes are not identical. While the field components of Yee's FDTD scheme represent the total field at a space point, the field components of the S-MRTD scheme represent only a part of the total field. In fact, the total field at a particular space

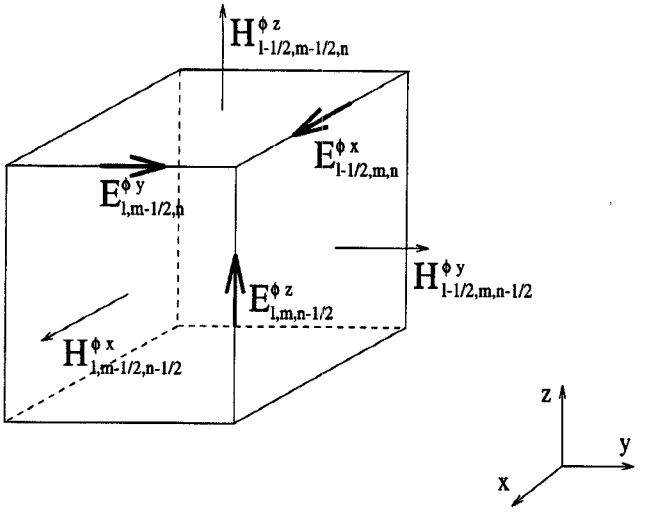

Fig. 3. Unit cell for the S-MRTD scheme.

point for the S-MRTD scheme may be calculated from the field expansions, see (6), by sampling them with delta test functions in space and time domain. For example, the x-component of the total electric field $E_x(\vec{r}_0, t_0) = E_x(x_0, y_0, z_0, t_0)$ at an arbitrary space point $\vec{r}_0$ at time t_0 with $(k-1/2)\Delta t < t_0 < (k+1/2)\Delta t$ is given by

$$\begin{aligned} E(\vec{r}_0, t_0) &= \iiint\!\!\int E_x(\vec{r}, t)\delta(x - x_0)\delta(y - y_0)\delta(z - z_0) \\ &\quad \cdot \delta(t - t_0)\, dx\, dy\, dz\, dt \\ &= \sum_{l',m',n'=-\infty}^{+\infty} {}_kE^{\phi x}_{l'+1/2,m',n'} \phi_{l'+1/2}(x_0)\phi_{m'}(y_0) \\ &\quad \cdot \phi_n{}'(z_0). \end{aligned} \tag{37}$$

Due to the exponentially decaying support of the Battle–Lemarie scaling function (see Fig. 1), only a few terms of this three-dimensional summation have to be considered.

B. Dispersion Analysis

Due to the discretization in space and time, the FDTD schemes exhibit deviations from the desired linear dispersion behavior. In order to estimate these deviations, the dispersion relation of a MRTD scheme has to be known. The method for the calculation of the dispersion relation is described in [19] and [20]. We use a general approach for the computation of the dispersion relation which is based on the state-space representation of the discretized electromagnetic field [8], [10]. Using this approach, the dispersion relation of the MRTD

$$\boldsymbol{M} = \begin{bmatrix} \varepsilon \boldsymbol{X}_h^\dagger \boldsymbol{T}_h^\dagger \boldsymbol{d}_t & 0 & 0 & 0 & \boldsymbol{T}_h^\dagger \boldsymbol{X}_h^\dagger \boldsymbol{D}_z^\phi & -\boldsymbol{T}_h^\dagger \boldsymbol{X}_h^\dagger \boldsymbol{D}_y^\phi \\ 0 & \varepsilon \boldsymbol{Y}_h^\dagger \boldsymbol{T}_h^\dagger \boldsymbol{d}_t & 0 & -\boldsymbol{T}_h^\dagger \boldsymbol{Y}_h^\dagger \boldsymbol{D}_z^\phi & 0 & \boldsymbol{T}_h^\dagger \boldsymbol{Y}_h^\dagger \boldsymbol{D}_x^\phi \\ 0 & 0 & \varepsilon \boldsymbol{Z}_h^\dagger \boldsymbol{T}_h^\dagger \boldsymbol{d}_t & \boldsymbol{T}_h^\dagger \boldsymbol{Z}_h^\dagger \boldsymbol{D}_y^\phi & -\boldsymbol{T}_h^\dagger \boldsymbol{Z}_h^\dagger \boldsymbol{D}_x^\phi & 0 \\ 0 & -\boldsymbol{Y}_h^\dagger \boldsymbol{Z}_h^\dagger \boldsymbol{D}_z^\phi & \boldsymbol{Y}_h^\dagger \boldsymbol{Z}_h^\dagger \boldsymbol{D}_y^\phi & \mu \boldsymbol{Y}_h^\dagger \boldsymbol{Z}_h^\dagger \boldsymbol{d}_t & 0 & 0 \\ \boldsymbol{X}_h^\dagger \boldsymbol{Z}_h^\dagger \boldsymbol{D}_z^\phi & 0 & -\boldsymbol{X}_h^\dagger \boldsymbol{Z}_h^\dagger \boldsymbol{D}_x^\phi & 0 & \mu \boldsymbol{X}_h^\dagger \boldsymbol{Z}_h^\dagger \boldsymbol{d}_t & 0 \\ -\boldsymbol{X}_h^\dagger \boldsymbol{Y}_h^\dagger \boldsymbol{D}_y^\phi & \boldsymbol{X}_h^\dagger \boldsymbol{Y}_h^\dagger \boldsymbol{D}_x^\phi & 0 & 0 & 0 & \mu \boldsymbol{X}_h^\dagger \boldsymbol{Y}_h^\dagger \boldsymbol{d}_t \end{bmatrix} \tag{36}$$

TABLE II
RESONANT FREQUENCIES FOR AN AIR-FILLED CAVITY

Analytic values	S-MRTD scheme (mesh size 2 × 4 × 3)		Yee's FDTD scheme (mesh size 10 × 20 × 15)	
	Absolute values	Relative error	Absolute values	Relative error
125.00 MHz	125.10 MHz	0.080 %	124.85 MHz	-0.120 %
180.27 MHz	180.50 MHz	0.128 %	179.75 MHz	-0.288 %
213.60 MHz	214.60 MHz	0.468 %	212.40 MHz	-0.562 %
246.22 MHz	248.70 MHz	1.007 %	244.50 MHz	-0.699 %
250.00 MHz	251.00 MHz	0.400 %	248.70 MHz	-0.520 %
301.04 MHz	303.90 MHz	0.950 %	298.95 MHz	-0.694 %
336.34 MHz	339.20 MHz	0.850 %	334.35 MHz	-0.592 %

scheme is calculated from the solutions of the eigenvalue problem in the field state-space.

The operator equation (35) requires

$$\det \boldsymbol{M}(\boldsymbol{T}_h, \boldsymbol{X}_h, \boldsymbol{Y}_h, \boldsymbol{Z}_h) = 0 \tag{38}$$

for any nontrivial solutions in the field state-space $\mathcal{H}_F$. Restricting the investigations to electromagnetic fields composed of plane waves, one obtains [10]

$$\det \boldsymbol{M}(e^{-\jmath\Omega/2}, e^{-\jmath\chi/2}, e^{-\jmath\eta/2}, e^{-\jmath\xi/2}) = 0 \tag{39}$$

where Ω is the normalized frequency related to the frequency f by $\Omega = 2\pi\Delta t f = \omega\Delta t$. The normalized wave vector components χ, η and ξ are related to the x-, y- and z-components of the wave vector $\vec{k}, k_x, k_y$ and k_z, by $\chi = \Delta l k_x, \eta = \Delta l k_y$ and $\xi = \Delta l k_z$. The evaluation of (39) yields

$$d_t(\Omega) = 0 \tag{40}$$

and

$$\varepsilon\mu(d_t(\Omega))^2 = (D_x^\phi(\chi))^2 + (D_y^\phi(\eta))^2 + (D_z^\phi(\xi))^2. \tag{41}$$

The difference operator in frequency domain, $d_t(\Omega)$, and the difference operators in wave vector domain, $D_x^\phi(\chi), D_y^\phi(\eta)$, and $D_z^\phi(\xi)$, are given by

$$d_t(\Omega) = \frac{1}{\Delta t}(e^{\jmath\Omega/2} - e^{-\jmath\Omega/2}) = \frac{2\jmath}{\Delta t}\sin(\Omega/2) \tag{42}$$

and

$$\begin{aligned} D_x^\phi(\chi) &= \frac{1}{\Delta x}\sum_{i=-9}^{+8} a(i) e^{\jmath\chi(i+1/2)} \\ &= \frac{2\jmath}{\Delta x}\sum_{i=0}^{+8} a(i)\sin\chi(i+1/2) \\ D_y^\phi(\eta) &= \frac{1}{\Delta y}\sum_{i=-9}^{+8} a(i) e^{\jmath\eta(i+1/2)} \\ &= \frac{2\jmath}{\Delta y}\sum_{i=0}^{+8} a(i)\sin\eta(i+1/2) \\ D_z^\phi(\xi) &= \frac{1}{\Delta z}\sum_{i=-9}^{+8} a(i) e^{\jmath\xi(i+1/2)} \\ &= \frac{2\jmath}{\Delta z}\sum_{i=0}^{+8} a(i)\sin\xi(i+1/2). \end{aligned} \tag{43}$$

Equation (40) represents the dispersion relation for the stationary solutions of the S-MRTD scheme corresponding to the electro- and magnetostatic solutions, since $d_t(\Omega) = 0$ implies $\Omega = 0$, while (41) represents the dispersion relation for the solutions propagating in the S-MRTD scheme. For small arguments, using $x \approx x$, (41) yields

$$\frac{\omega^2}{c^2} \approx k_x^2 + k_y^2 + k_z^2 \tag{44}$$

which corresponds to the exact linear dispersion relation, when all coefficients $a(i)$ are considered. In this case, (44) is identical to the dispersion relation of a three-dimensional wave equation with the wave propagation velocity c.

While the stability condition for Yee's FDTD scheme for a uniform discretization with $\Delta x = \Delta y = \Delta z = \Delta l$ is given by [1]

$$\Delta t \le \frac{1}{\sqrt{3}}\frac{\Delta l}{c} = 0.57735\frac{\Delta l}{c} \tag{45}$$

the stability condition for the S-MRTD scheme results in

$$\Delta t \le \Delta t_{\max} = 0.368112\frac{\Delta l}{c}. \tag{46}$$

The latter condition may be derived by requiring that for all wave vectors, (41) must have a solution for real frequencies Ω in order to obtain a stable MRTD scheme.

Figs. 4–6 illustrate the highly linear dispersion characteristics of the S-MRTD scheme in comparison with the dispersion characteristics of Yee's FDTD scheme [19] for uniform discretization. For wave propagation in (1, 0, 0) direction and along the x-axis, respectively, we have used $\eta = 0$ and $\xi = 0$. Similarly, for wave propagation in (1, 1, 0) direction and along the diagonal in the x-y-plane, respectively, we have used $\chi = \eta$ and $\xi = 0$ as well as $\chi = \eta = \xi$ for wave propagation in (1, 1, 1) direction. In contrast to Yee's FDTD scheme, it is not advantageous to choose Δt at the stability limit but at about five times less. With this choice, much more linearity of the dispersion characteristics is achieved. In order to illustrate this linearity, in Figs. 4–6, the same $\Delta t = \Delta t_{\max}/5$ has been chosen for both schemes.

The benefits of the highly linear dispersion characteristics are illustrated in Table II, which shows the results for the resonant frequencies of an air-filled cavity. The cavity has the dimensions 1m × 2m × 1.5m. For the analysis using Yee's

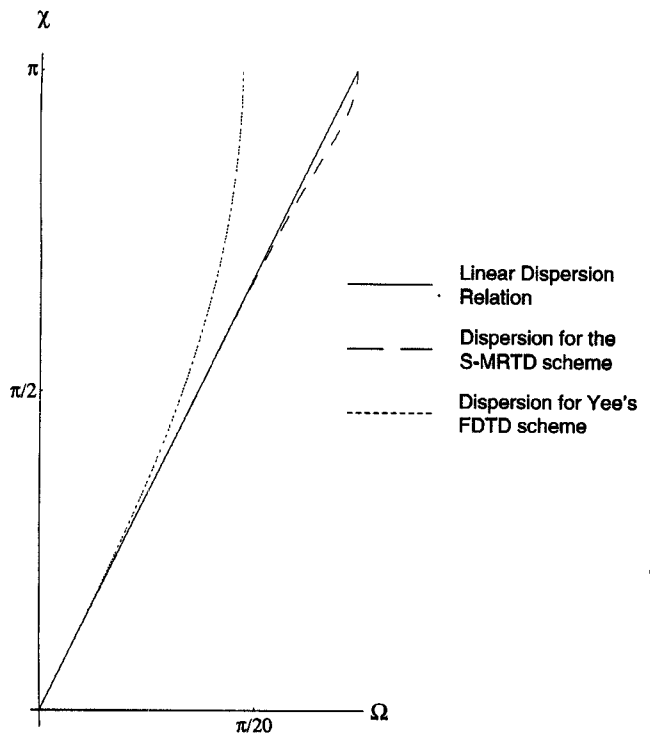

Fig. 4. Dispersion diagram for S-MRTD for propagation in (1, 0, 0) direction.

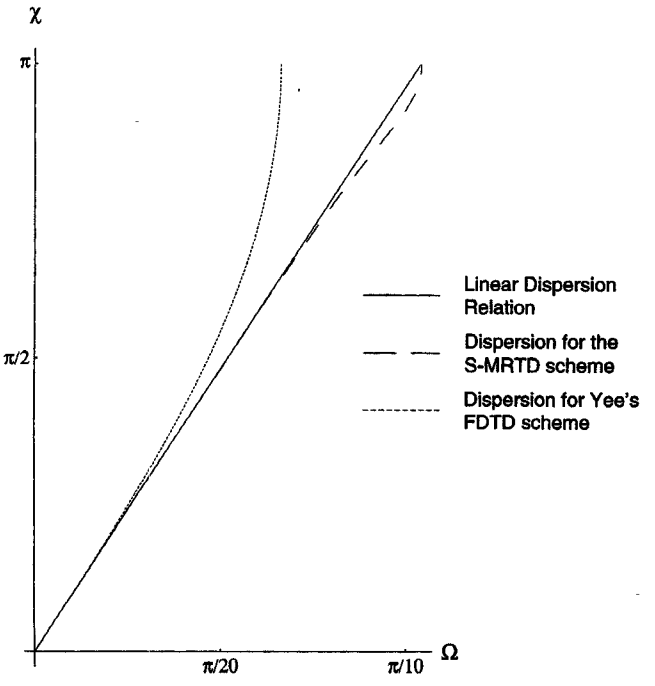

Fig. 5. Dispersion diagram for S-MRTD for propagation in (1, 1, 0) direction.

FDTD scheme, a mesh with $\Delta l = 0.1$ m was used resulting in a total number of 3000 grid points. Analyzing the cavity with the S-MRTD scheme, a mesh with $\Delta l = 0.5$m and with 24 grid points, respectively, was chosen reducing the total number of grid points by a factor of 125. Furthermore, the execution time for the analysis was reduced by a factor of nine to ten using the

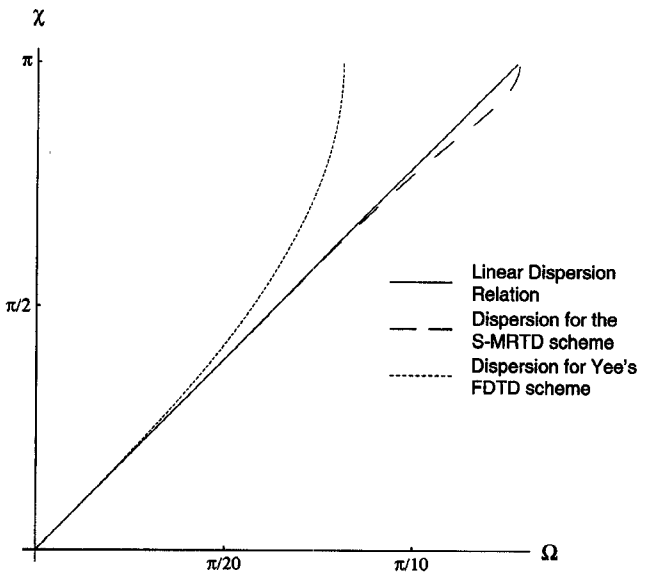

Fig. 6. Dispersion diagram for S-MRTD for propagation in (1, 1, 1) direction.

S-MRTD scheme instead of Yee's FDTD scheme. Note that the time discretization interval $\Delta t = 10^{-10}$ s was chosen to be identical for both schemes in order to exploit the linearity of the dispersion characteristics for S-MRTD. In addition, note that for the S-MRTD scheme, the relative error of the resonant frequencies is always positive which corresponds to an overestimation of the resonant frequencies. For Yee's FDTD scheme, the relative error of the resonant frequencies is always negative corresponding to an underestimation of the resonant frequencies. This is exactly what has to be expected from the dispersion diagrams, see Figs. 4–6.

Since the use of nonlocalized basis functions does not allow localized boundary conditions, the perfect electric boundary conditions in a S-MRTD mesh are modeled using the image principle. This means that the perfect electric conductor (PEC) is replaced by an open structure with symmetric electromagnetic fields. In particular, the electric field components tangential to the PEC must have uneven symmetry in order to ensure a field distribution with zero tangential electric fields at the original position of the PEC. Furthermore, the magnetic field components tangential to the PEC must have even symmetry with respect to the original position of the PEC. In the same way, perfect magnetic conductors (PMC's) may be modeled assuming uneven tangential magnetic fields and even tangential electric fields with respect to the PMC.

III. W-MRTD Schemes

In order to incorporate wavelets in the S-MRTD scheme, we consider an additional term in the electromagnetic field expansions using a set of wavelet functions. For simplicity, we will consider wavelet expansion in one dimension and in one resolution level only. Considering the wavelets for the other dimensions and for the higher resolution levels is straightforward. In particular, we will use additional wavelet

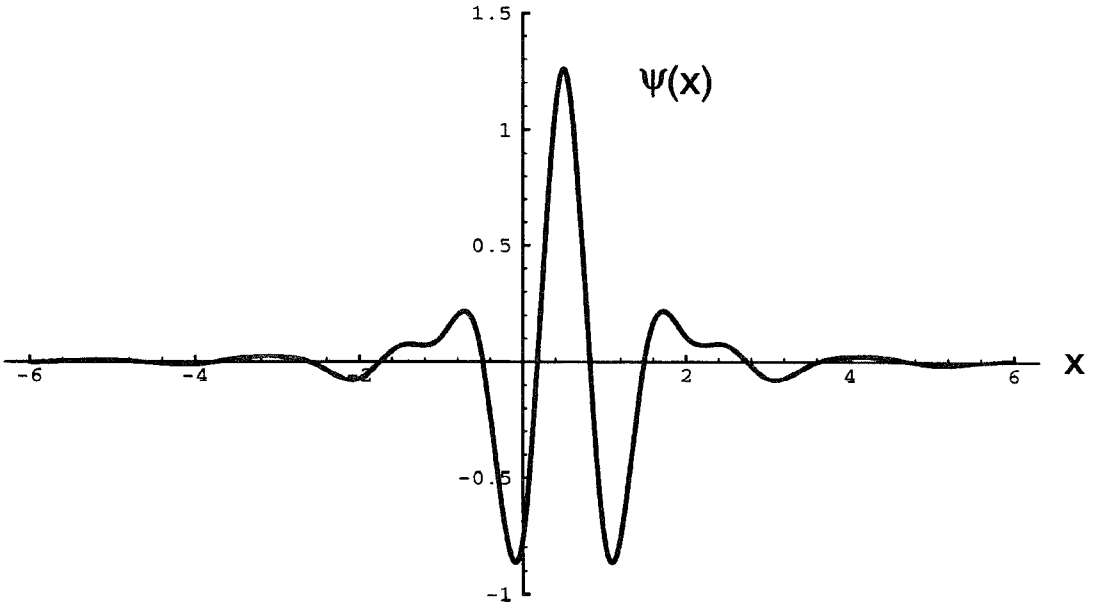

Fig. 7. Cubic spline Battle–Lemarie wavelet function in space domain.

functions with respect to the y-coordinate. In the following, the FDTD scheme derived by this field expansion is denoted by Wy-MRTD scheme.

A. Derivation of the Wy-MRTD Scheme

In the following, we replace the expansions of the field components, (6), by a two-fold expansion in scaling functions and wavelet functions with respect to the y-coordinate. Thus we expand the field components as following

$$E_x(\vec{r},t) = \sum_{k,l,m,n=-\infty}^{+\infty} ({}_kE^{\phi x}_{l+1/2,m,n}\phi_m(y) + {}_kE^{\psi x}_{l+1/2,m+1/2,n}\psi_{m+1/2}(y)) \cdot h_k(t)\phi_{l+1/2}(x)\phi_n(z)$$

$$E_y(\vec{r},t) = \sum_{k,l,m,n=-\infty}^{+\infty} ({}_kE^{\phi y}_{l,m+1/2,n}\phi_m(y) + {}_kE^{\psi y}_{l,m,n}\psi_m(y))h_k(t)\phi_l(x)\phi_n(z)$$

$$E_z(\vec{r},t) = \sum_{k,l,m,n=-\infty}^{+\infty} ({}_kE^{\phi z}_{l,m,n+1/2}\phi_m(y) + {}_kE^{\psi z}_{l,m+1/2,n+1/2}\psi_{m+1/2}(y)) \cdot h_k(t)\phi_l(x)\phi_{n+1/2}(z)$$

$$H_x(\vec{r},t) = \sum_{k,l,m,n=-\infty}^{+\infty} ({}_{k+1/2}H^{\phi x}_{l,m+1/2,n+1/2} \cdot \phi_{m+1/2}(y) + {}_{k+1/2}H^{\psi x}_{l,m,n+1/2}\psi_m(y)) \times h_{k+1/2}(t)\phi_l(x)\phi_{n+1/2}(z)$$

$$H_y(\vec{r},t) = \sum_{k,l,m,n=-\infty}^{+\infty} ({}_{k+1/2}H^{\phi y}_{l+1/2,m,n+1/2}\phi_m(y) + {}_{k+1/2}H^{\psi y}_{l+1/2,m+1/2,n+1/2}\psi_{m+1/2}(y)) \times h_{k+1/2}(t)\phi_{l+1/2}(x)\phi_{n+1/2}(z)$$

$$H_z(\vec{r},t) = \sum_{k,l,m,n=-\infty}^{+\infty} ({}_{k+1/2}H^{\phi z}_{l+1/2,m+1/2,n}\phi_{m+1/2}(y) + {}_{k+1/2}H^{\psi z}_{l+1/2,m,n}\psi_m(y)) \times h_{k+1/2}(t)\phi_{l+1/2}(x)\phi_n(z) \quad (47)$$

where ${}_kE^{\psi\kappa}_{l,m,n}$ and ${}_kH^{\psi\kappa}_{l,m,n}$ with $\kappa = x, y, z$ are the expansion coefficients for the field expansions in terms of wavelet functions. The function $\psi_{m+1/2}(x)$ is defined as

$$\psi_{m+1/2}(x) = \psi\Big(\frac{x}{\Delta x} - m\Big) \quad (48)$$

where $\psi(x)$ represents the cubic spline Battle–Lemarie wavelet function [13], [14] depicted in Fig. 7. Note that the scaling function has an even symmetry with respect to $x = 0$, whereas the wavelet function has an even symmetry with respect to $x = 1/2$. This is the reason why we have denoted the expansion coefficients for the wavelet expansions with an index $m' = m + 1/2$, where m represents the index for the scaling function expansion coefficients. Note that in order to include the resolution level t, one has to add the expansion in terms of the wavelet functions

$$\psi_{s,m+1/2}(x) = 2^{s/2}\psi\Big(2^s\frac{x}{\Delta x} - m\Big) \quad (49)$$

with $s = 1, 2, \cdots, t$.

The closed form expression of the wavelet function in spectral domain is given by [17]

$$\tilde{\psi}(\lambda) = e^{\jmath\lambda/2}\frac{\tilde{\phi}(\lambda+2\pi)}{\tilde{\phi}(\lambda/2+\pi)}\tilde{\phi}(\lambda/2) = \frac{e^{\jmath\lambda/2}\left(\frac{2}{\lambda}\sin\left(\frac{\lambda}{2}\right)\tan\left(\frac{\lambda}{2}\right)\right)^4}{\sqrt{1-\frac{4}{3}\sin^2\left(\frac{\lambda}{2}\right)+\frac{2}{5}\sin^4\left(\frac{\lambda}{2}\right)-\frac{4}{315}\sin^6\left(\frac{\lambda}{2}\right)}}$$

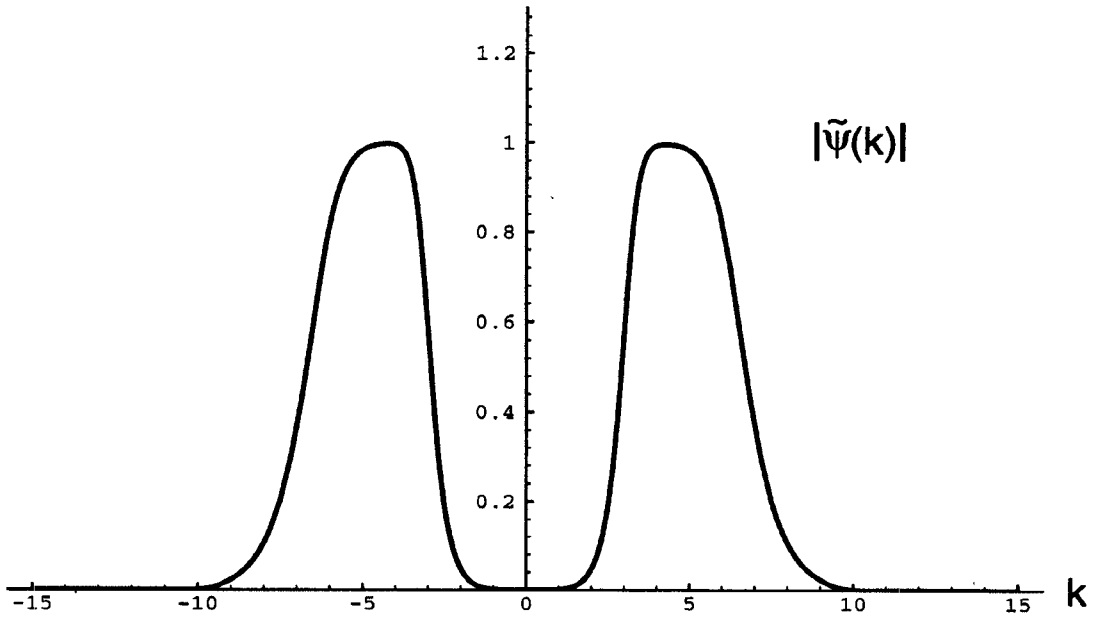

Fig. 8. Magnitude of the cubic spline Battle–Lemarie wavelet function in spectral domain.

$$\cdot\sqrt{\frac{1-\frac{4}{3}\cos^2\left(\frac{\lambda}{4}\right)+\frac{2}{5}\cos^4\left(\frac{\lambda}{4}\right)-\frac{4}{315}\cos^6\left(\frac{\lambda}{4}\right)}{1-\frac{4}{3}\sin^2\left(\frac{\lambda}{4}\right)+\frac{2}{5}\sin^4\left(\frac{\lambda}{4}\right)-\frac{4}{315}\sin^6\left(\frac{\lambda}{4}\right)}}. \tag{50}$$

Fig. 8 exhibits the band-pass characteristics of the wavelet function. In the interval $|\lambda| < 2$, the magnitude of the function $\tilde{\psi}(k)$ is nearly zero. Thus in this interval, the scaling function alone yields a correct representation of the electromagnetic fields which is reflected in the dispersion characteristics of the S-MRTD and Wy-MRTD scheme. It will be shown in the next subsection that for a large frequency interval, the dispersion characteristics of both MRTD schemes exhibit no dispersion error and no deviation from the linear dispersion relation, respectively. However near discontinuities, the electromagnetic fields contain parts with higher spectral frequencies which calls for additional wavelets to be taken into account in order to calculate the fields correctly.

Again, we insert the field expansions in Maxwell's equations and sample the equations using pulse functions as test functions in time. With respect to space, we use scaling and wavelet functions as test functions. In addition to the integrals (13), (15), (16), and (19), we need to apply the orthogonality relations [17]

$$\int_{-\infty}^{+\infty} \psi_m(x)\psi_{m'}(x)\,dx = \delta_{m,m'}\Delta x \tag{51}$$

and

$$\int_{-\infty}^{+\infty} \phi_m(x)\psi_{m'+1/2}(x)\,dx = 0. \tag{52}$$

Furthermore, using the closed form expressions of the scaling and wavelet function in spectral domain, (12) and (50) requires the calculation of the integrals

$$\begin{aligned}
&\int_{-\infty}^{+\infty} \psi_m(x)\frac{\partial\psi_{m'+1/2}(x)}{\partial x}\,dx \\
&\quad = \frac{1}{\pi}\int_0^{\infty} |\tilde{\psi}(\lambda)|^2\lambda\sin\lambda(m'+1/2-m)\,d\lambda \\
&\int_{-\infty}^{+\infty} \phi_m(x)\frac{\partial\psi_{m'+1/2}(x)}{\partial x}\,dx \\
&\quad = \frac{1}{\pi}\int_0^{\infty} \tilde{\phi}(\lambda)|\tilde{\psi}(\lambda)|\lambda\sin\lambda(m'+1-m)\,d\lambda \\
&\int_{-\infty}^{+\infty} \psi_m(x)\frac{\partial\phi_{m'}(x)}{\partial x}\,dx \\
&\quad = \frac{1}{\pi}\int_0^{\infty} \tilde{\phi}(\lambda)|\tilde{\psi}(\lambda)|\lambda\sin\lambda(m'-m)\,d\lambda.
\end{aligned} \tag{53}$$

These integrals may again be evaluated numerically resulting in the approximations

$$\begin{aligned}
&\int_{-\infty}^{+\infty} \psi_m(x)\frac{\partial\psi_{m'+1/2}(x)}{\partial x}\,dx \approx \sum_{i=-9}^{+8} b(i)\delta_{m+i,m'} \\
&\int_{-\infty}^{+\infty} \phi_m(x)\frac{\partial\psi_{m'+1/2}(x)}{\partial x}\,dx \approx \sum_{i=-9}^{+9} c(i)\delta_{m+i,m'+1} \\
&\int_{-\infty}^{+\infty} \psi_m(x)\frac{\partial\phi_{m'}(x)}{\partial x}\,dx \approx \sum_{i=-9}^{+9} c(i)\delta_{m+i,m'}
\end{aligned} \tag{54}$$

where the coefficients $b(i)$ and $c(i)$ for $0 \le i \le 8$ are shown in Table III. The coefficients $b(i)$ and $c(i)$ for $i < 0$ are given by the symmetry relations $b(-1-i) = -b(i)$ and $c(-i) = -c(i)$. Due to the exponentially decaying support of the Battle–Lemarie scaling and wavelet function, the coefficients $b(i)$ for $i > 8$ and $c(i)$ for $i > 9$ do not affect the accuracy of the field computation significantly.

As an example, let us again consider the discretization of (2). Sampling the term on the right side, $\partial E_x/\partial t$, with scaling

TABLE III
THE COEFFICIENTS $b(i)$ AND $c(i)$

i	$b(i)$	$c(i)$
0	2.4725388	0.0
1	0.9562282	-0.0465973
2	0.1660587	0.0545394
3	0.0939244	-0.0369996
4	0.0031413	0.0205745
5	0.0134936	-0.0111530
6	-0.0028589	0.0059769
7	0.0027788	-0.0032026
8	-0.0011295	0.0017141
9		-0.0009177

functions in space and pulse functions in time yields

$$\iiiint \frac{\partial E_x}{\partial t}\phi_{l+1/2}(x)\phi_m(y)\phi_n(z)h_{k+1/2}(t)\,dx\,dy\,dz\,dt = ({}_{k+1}E^{\phi z}_{l+1/2,m,n} - {}_kE^{\phi z}_{l+1/2,m,n})\Delta x\Delta y\Delta z. \quad (55)$$

Sampling the same term using wavelet functions with respect to the y-coordinate and scaling functions in space domain as well as pulse functions in time domain yields

$$\iiiint \frac{\partial E_x}{\partial t}\phi_{l+1/2}(x)\psi_{m+1/2}(y)\phi_n(z)h_{k+1/2}(t)\,dx\,dy\,dz\,dt = ({}_{k+1}E^{\psi z}_{l+1/2,m+1/2,n} - {}_kE^{\psi z}_{l+1/2,m+1/2,n})\Delta x\Delta y\Delta z. \quad (56)$$

Applying the same test functions in order to discretize $\partial H_z/\partial y$, we obtain

$$\iiiint \frac{\partial H_z}{\partial y}\phi_{l+1/2}(x)\phi_m(y)\phi_n(z)h_{k+1/2}(t)\,dx\,dy\,dz\,dt = \left(\sum_{i=-9}^{+8} a(i)_{k+1/2}H^{\phi z}_{l+1/2,m+i+1/2,n} + \sum_{i=-9}^{+9} c(i)_{k+1/2}H^{\psi z}_{l+1/2,m+i,n}\right)\Delta x\Delta z\Delta t \quad (57)$$

and

$$\iiiint \frac{\partial H_z}{\partial y}\phi_{l+1/2}(x)\psi_{m+1/2}(y)\phi_n(z)h_{k+1/2}(t)\,dx\,dy\,dz\,dt = \left(\sum_{i=-9}^{+9} c(i)_{k+1/2}H^{\phi z}_{l+1/2,m+i+1/2,n} + \sum_{i=-9}^{+8} b(i)_{k+1/2}H^{\psi z}_{l+1/2,m+i+1,n}\right)\Delta x\Delta z\Delta t. \quad (58)$$

We proceed in the same way with the term $\partial H_y/\partial z$ and obtain the two difference equations

$$\frac{\varepsilon}{\Delta t}({}_{k+1}E^{\phi x}_{l+1/2,m,n} - {}_kE^{\phi x}_{l+1/2,m,n}) = \frac{1}{\Delta y}\sum_{i=-9}^{+8} a(i)_{k+1/2}H^{\phi z}_{l+1/2,m+i+1/2,n} + \frac{1}{\Delta y}\sum_{i=-9}^{+9} c(i)_{k+1/2}H^{\psi z}_{l+1/2,m+i,n} - \frac{1}{\Delta z}\sum_{i=-9}^{+8} a(i)_{k+1/2}H^{\phi y}_{l+1/2,m,n+i+1/2} \quad (59)$$

and

$$\frac{\varepsilon}{\Delta t}({}_{k+1}E^{\psi x}_{l+1/2,m+1/2,n} - {}_kE^{\phi x}_{l+1/2,m+1/2,n}) = \frac{1}{\Delta y}\sum_{i=-9}^{+9} c(i)_{k+1/2}H^{\phi z}_{l+1/2,m+i+1/2,n} + \frac{1}{\Delta y}\sum_{i=-9}^{+8} b(i)_{k+1/2}H^{\psi z}_{l+1/2,m+i+1,n} - \frac{1}{\Delta z}\sum_{i=-9}^{+8} a(i)_{k+1/2}H^{\psi y}_{l+1/2,m+1/2,n+i+1/2}. \quad (60)$$

Defining the electric and magnetic field component vectors

$$|E_{\psi\kappa}\rangle = \sum_{k,l,m,n=-\infty}^{+\infty} {}_kE^{\psi\kappa}_{l,m,n}|k;l,m,n\rangle \quad (61)$$

and

$$|H_{\psi\kappa}\rangle = \sum_{k,l,m,n=-\infty}^{+\infty} {}_kH^{\psi\kappa}_{l,m,n}|k;l,m,n\rangle \quad (62)$$

with $\kappa = x, y, z$ as vectors in $\mathcal{H}_{m\otimes t}$, we can represent (59) and (60) by the operator equations

$$\varepsilon \boldsymbol{X}_h^\dagger \boldsymbol{T}_h^\dagger \boldsymbol{d}_t|E_{\phi x}\rangle = \boldsymbol{X}_h^\dagger \boldsymbol{T}_h^\dagger(\boldsymbol{D}_y^\phi|H_{\phi z}\rangle + \boldsymbol{D}_y^I|H_{\psi z}\rangle - \boldsymbol{D}_z^\phi|H_{\phi y}\rangle) \quad (63)$$

and

$$\varepsilon \boldsymbol{X}_h^\dagger \boldsymbol{Y}_h^\dagger \boldsymbol{T}_h^\dagger \boldsymbol{d}_t|E_{\psi x}\rangle = \boldsymbol{X}_h^\dagger \boldsymbol{Y}_h^\dagger \boldsymbol{T}_h^\dagger(\boldsymbol{D}_y^I|H_{\phi z}\rangle + \boldsymbol{D}_y^\psi|H_{\psi z}\rangle - \boldsymbol{D}_z^\phi|H_{\psi y}\rangle). \quad (64)$$

The difference operators $\boldsymbol{D}_y^\psi$ and $\boldsymbol{D}_y^I$ are defined as

$$\boldsymbol{D}_y^\psi = \frac{1}{\Delta y}\boldsymbol{Y}_h^\dagger \sum_{i=-9}^{+8} b(i)\boldsymbol{Y}^{-i}$$

$$\boldsymbol{D}_y^I = \frac{1}{\Delta y}\sum_{i=-9}^{+9} c(i)\boldsymbol{Y}^{-i}. \quad (65)$$

Since the operator $\boldsymbol{D}_y^I$ describes the interaction between the scaling and wavelet function expansion coefficients, we use the index I to denote this operator. Proceeding in the same way with the five remaining scalar cartesian Maxwell's equations, we obtain another ten different equations.

The unit cell of the Wy-MRTD scheme is depicted in Fig. 9. The number of independent field variables per unit cell is twelve which is twice as much as for Yee's FDTD scheme and the S-MRTD scheme. The total field at a particular space point for the Wy-MRTD scheme may be calculated from the field expansions (47) by sampling the expansions using delta test functions in space and time domain, e.g., the x-component

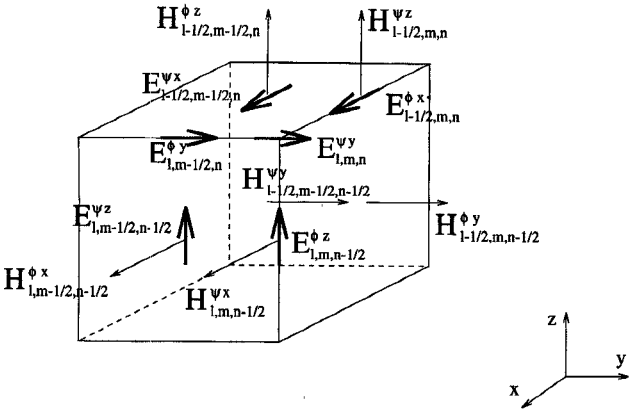

Fig. 9. Unit cell for the Wy-MRTD scheme.

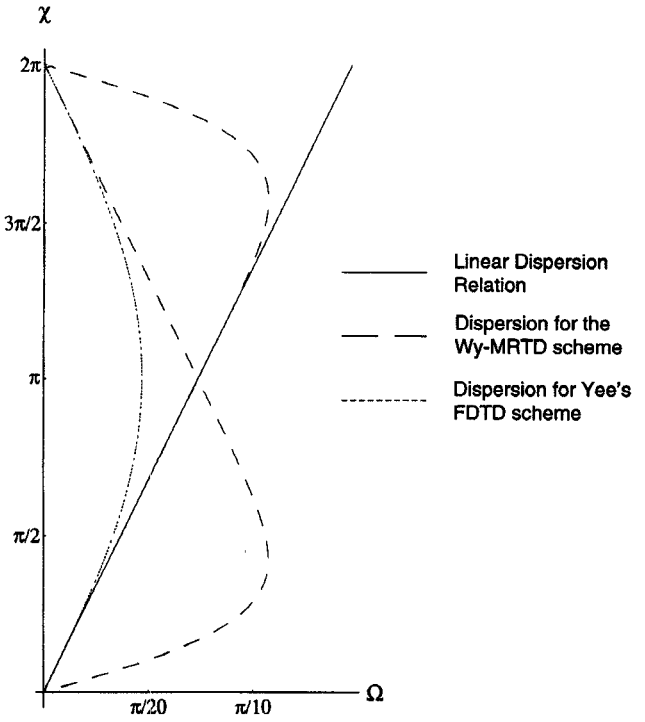

Fig. 10. Dispersion diagram for Wy-MRTD for propagation in (0, 1, 0) direction.

of the total electric field $E_x(\vec{r}_0, t_0)$ at the arbitrary space point $\vec{r}_0$ at time t_0 with $(k-1/2)\Delta t < t_0 < (k+1/2)\Delta t$ is given by

$$\begin{aligned} E(\vec{r}_0, t_0) &= \iiint\!\!\iint E_x(\vec{r}, t)\delta(x - x_0)\delta(y - y_0)\delta(z - z_0) \\ &\quad \cdot \delta(t - t_0)\, dx\, dy\, dz\, dt \\ &= \sum_{l',m',n'=-\infty}^{+\infty} ({}_kE^{\phi x}_{l'+1/2,m',n'}\phi_{m'}(y_0) \\ &\quad + {}_kE^{\psi x}_{l'+1/2,m'+1/2,n'}\psi_{m'+1/2}(y_0)) \\ &\quad \cdot \phi_{l'+1/2}(x_0)\phi_{n'}(z_0) \end{aligned} \tag{66}$$

where, due to the exponentially decaying support of the Battle–Lemarie scaling and wavelet functions (see Figs. 1 and 7), only a few terms of the three-dimensional summation have to be considered.

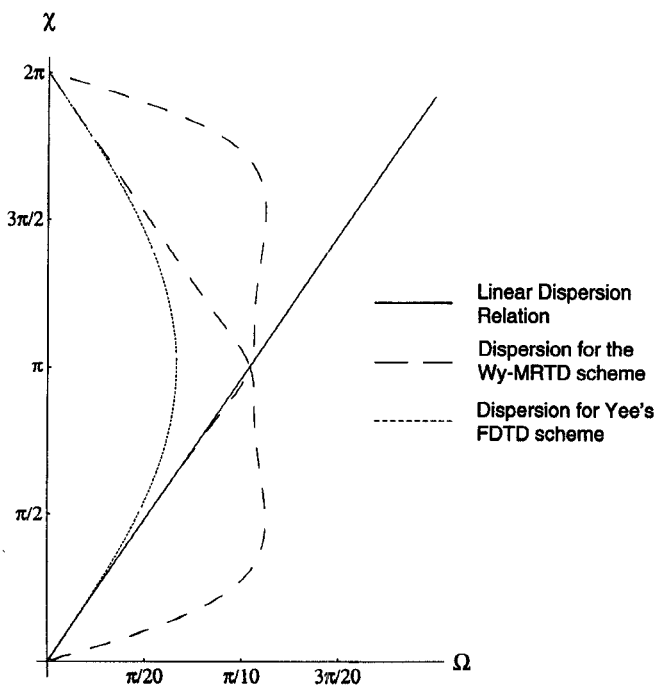

Fig. 11. Dispersion diagram for Wy-MRTD for propagation in (1, 1, 0) direction.

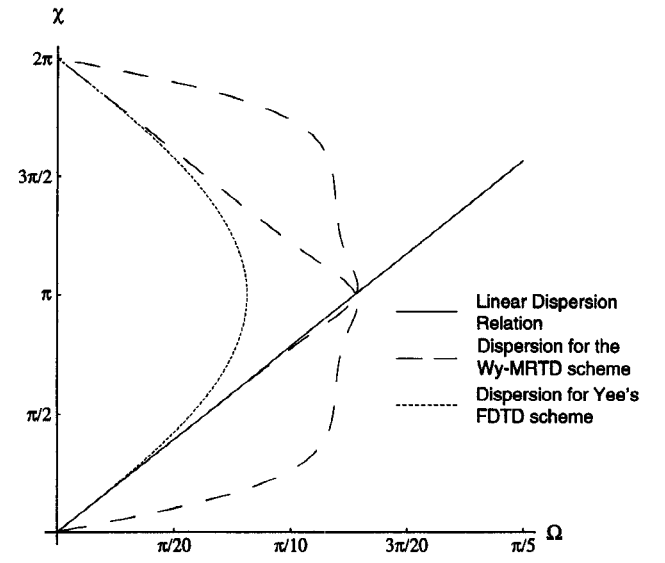

Fig. 12. Dispersion diagram for Wy-MRTD for propagation in (1, 1, 1) direction.

B. Dispersion Analysis

For the evaluation of (39), we have to calculate the determinant of a 12 × 12 matrix resulting in

$$d_t(\Omega) = 0 \tag{67}$$

and

$$\begin{aligned} &\varepsilon^2\mu^2(d_t(\Omega))^4 - \varepsilon\mu(d_t(\Omega))^2(2D^2_{xz}(\chi,\xi) + D^2_y(\eta)) \\ &\quad + (D^2_{xz}(\chi,\xi))^2 + D^2_{xz}(\chi,\xi)D^2_y(\eta) + (D^I_y(\eta))^4 \\ &\quad - 2D^\phi_y(\eta)D^\psi_y(\eta)(D^I_y(\eta))^2 + (D^\phi_y(\eta)D^\psi_y(\eta))^2 = 0 \end{aligned} \tag{68}$$

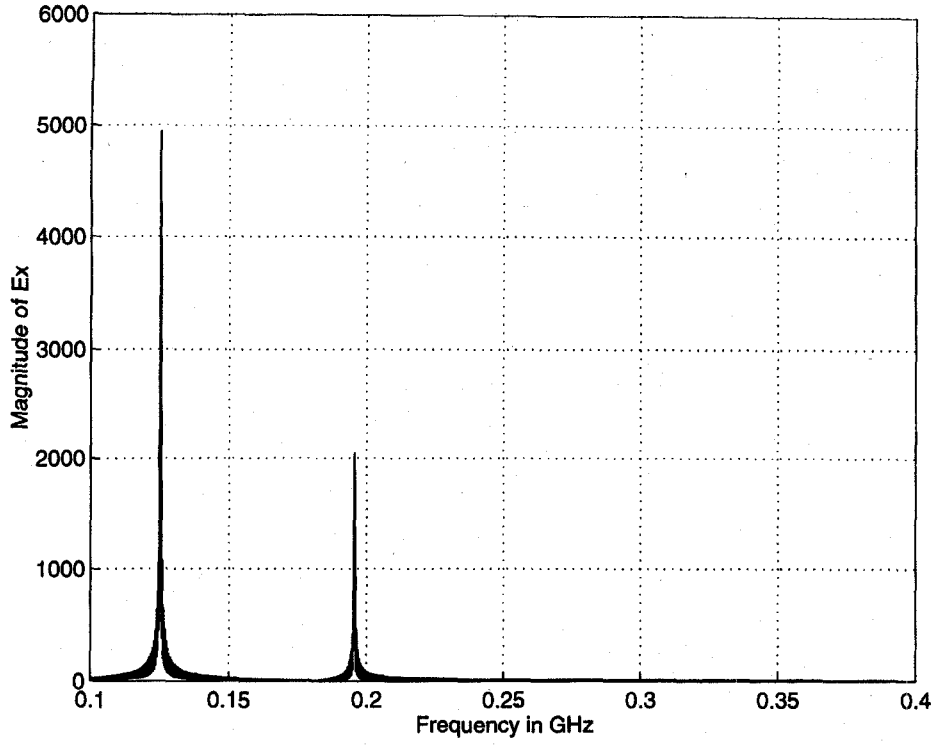

Fig. 13. Magnitude of the x-component of the electric field in frequency domain calculated by S-MRTD.

with

$$D_y^2(\eta) = (D_y^{\phi}(\eta))^2 + 2(D_y^I(\eta))^2 + (D_y^{\psi}(\eta))^2 \tag{69}$$

and

$$D_{xz}^2(\chi,\xi) = (D_x^{\phi}(\chi))^2 + (D_z^{\phi}(\xi))^2. \tag{70}$$

The difference operators D_y^{ψ} and D_y^I in wave vector domain are given by

$$D_y^{\psi} = \frac{2\jmath}{\Delta y}\sum_{i=0}^{8} b(i)\sin\eta(i+1/2)$$

$$D_y^I = \frac{2\jmath}{\Delta y}\sum_{i=1}^{9} c(i)\sin\eta i. \tag{71}$$

Equation (67) represents the dispersion relation for the stationary solutions of the Wy-MRTD scheme corresponding to the electro- and magnetostatic solutions, while (68) represents the dispersion relation for the solutions propagating in the Wy-MRTD scheme. For small arguments, using $x \approx x$ and considering all coefficients $a(i), b(i)$ and $c(i)$, (68) yields

$$\left(\frac{\omega^2}{c^2} - k_x^2 - k_y^2 - k_z^2\right)\left(\frac{\omega^2}{c^2} - k_x^2 - 49k_y^2 - k_z^2\right) = 0 \tag{72}$$

indicating the existence of spurious modes similar to those in the TLM scheme with symmetrical condensed node [21], [22].

Choosing a uniform discretization, the stability condition for the W-MRTD scheme based on wavelet functions in all three dimensions is given by

$$\Delta t \leq 0.253064\frac{\Delta l}{c}. \tag{73}$$

Figs. 10–12 illustrate the effect of adding wavelets with respect to the y-coordinate. To keep all dispersion diagrams consistent, for the W-MRTD and for the FDTD scheme, we have chosen the same $\Delta t = \Delta t_{\max}/5$ as in Figs. 4–6. In contrast to the dispersion diagrams shown in the previous section, we have depicted the curves for the whole period of the normalized wave vector component in order to give a better insight in the nature of the dispersion curves. For wave propagation in (0, 1, 0) direction and along the y-axis, respectively, we have used $\chi = 0$ and $\xi = 0$. Since there are no wavelets in the direction of the x-axis, the dispersion diagram for wave propagation in (1, 0, 0) direction is identical to Fig. 4. The use of wavelets with respect to the y-coordinate results in a further increase of linearity of the dispersion relation for wave propagation in this direction. However, there is now a second branch of the dispersion curve in the interval $0 < \xi < \pi$ and $0 < \Omega < \pi$ which is necessary to maintain the symmetry of the dispersion curve with respect to χ. This second branch causes unphysical or spurious solutions for small frequencies and small wave vectors as indicated by (72).

To demonstrate the existence of the spurious modes, we analyze the same cavity as in the previous section. However, to keep things simple, we choose a mesh with $\Delta x = 0.5$m, $\Delta y = 1$ m and $\Delta z = 0.75$ m resulting in a mesh with only eight grid points. Figs. 13 and 14 depict the magnitude of the x-component of the electric field in frequency domain calculated by S-MRTD and Wy-MRTD. Since for the S-MRTD mesh, there is only one x-component of the electric field in the direction of the y- and z-axis, only the $\mathrm{TE}_{0,1,1}$ and $\mathrm{TE}_{1,1,1}$ mode can be detected. However, the accuracy of the resonant frequencies is still excellent. For the first resonant frequency, the numerical value is 125.15 MHz and the relative error

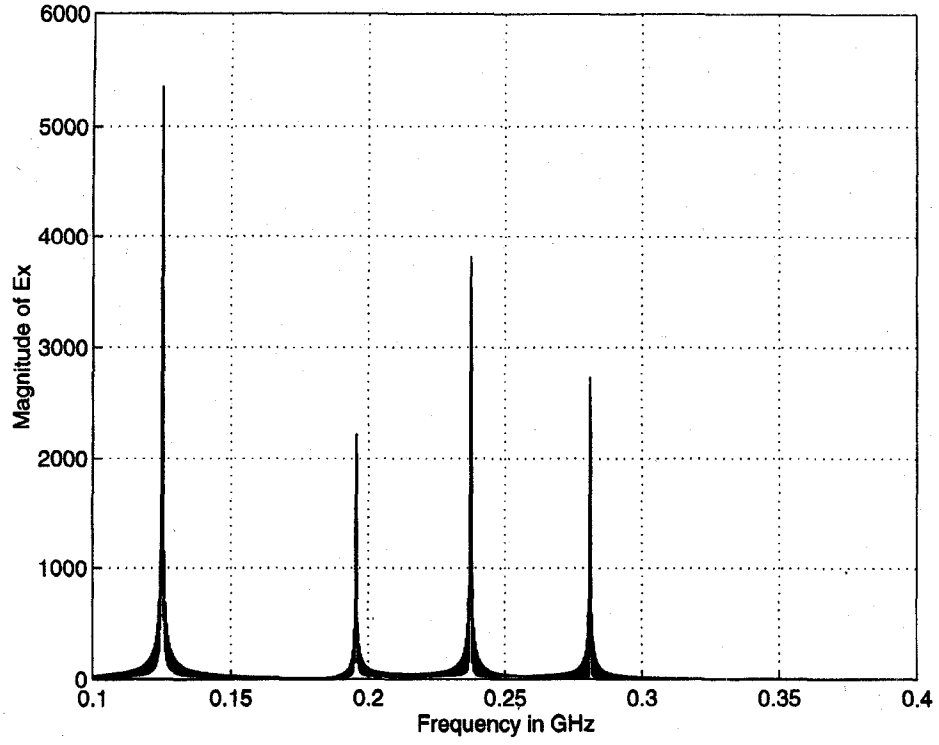

Fig. 14. Magnitude of the x-component of the electric field in frequency domain calculated by Wy-MRTD.

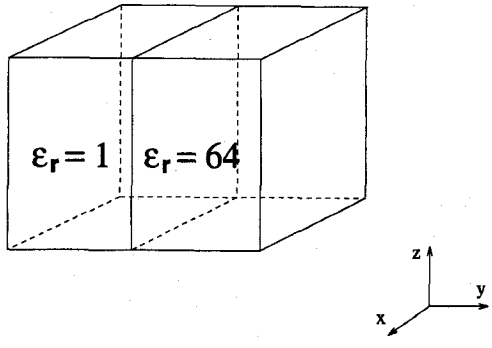

Fig. 15. Cavity half-filled with dielectric material.

0.12%. For the second resonant frequency, the numerical value is 195.6 MHz and the relative error 0.176%. Note that for the $TE_{1,1,1}$ mode, the electromagnetic fields are modeled by a minimum of discretization points. E.g. for the x-component of the electric field, the field distributions in y- and z-direction are modeled by one field component and the field distribution in x-direction by only two. Thus the result for this resonant frequency demonstrates the capability of achieving excellent accuracy for a ratio of the space discretization interval and the wavelength close to one over two and close to the Nyquist sampling limit, respectively.

The results for the Wy-MRTD scheme include another two resonant frequencies. These two resonant frequencies represent solutions which are spurious as it can be proven using the dispersion relation (68). Inserting the values for the wave vector components of the $TE_{0,1,1}$ mode, the dispersion relation yields the two frequencies 125.15 MHz and 237.42 MHz, which are identical with the numerical results of 125.15 MHz and 237.40 MHz. The same identity holds for the $TE_{1,1,1}$ mode, for which the dispersion relation yields 195.57 MHz and 281.10 MHz and the numerical analysis 195.55 MHz and 281.10 MHz.

Note that the relative error for the resonant frequency of the $TE_{0,1,1}$ mode is identical for both FDTD schemes, whereas for the $TE_{1,1,1}$ mode, there is a slight improvement to a relative error of 0.151% for the Wy-MRTD scheme. This is in agreement with the dispersion diagrams: For a frequency interval up to the cutoff frequency of Yee's FDTD scheme [10], the dispersion characteristics of the S-MRTD and Wy-MRTD schemes exhibit no dispersion error and no deviation from the linear dispersion relation, respectively. For larger frequencies, the dispersion error is slightly less for the Wy-MRTD scheme. However, this small improvement with respect to the accuracy of the resonant frequencies is offset by the increase in computer memory by a factor of two and the increase in execution time by a factor of 3.6. This increase in computer resources and the existence of spurious solutions in an infinite W-MRTD mesh indicate that wavelets should only be used locally in regions characterized by strong field variations or field singularities. In the next section, we will demonstrate the benefits of additional wavelets by analyzing a microwave structure with a discontinuity of the material properties.

IV. Modelling Symmetric Anisotropic Dielectric Media

In order to model symmetric anisotropic dielectric media, we separate Maxwell's first vector equation (1) in

$$\nabla \times \boldsymbol{H} = \frac{\partial \boldsymbol{D}}{\partial t} \tag{74}$$

and

$$\boldsymbol{D} = \varepsilon(\vec{r}, t)\boldsymbol{E} \tag{75}$$

where $\boldsymbol{D}$ represents the electric flux vector and $\varepsilon(\vec{r}, t)$ the space- and time-dependent permittivity tensor. Equation (74) together with (5) is discretized as described in the two previous sections. In the following, we will describe how to discretize (75) using the method of moments. Note that symmetric anisotropic magnetic media may be treated in the same way by separating Maxwell's second equation (5) in one partial differential equation and one equation describing the material properties.

In the principal coordinate system, the permittivity tensor ε for symmetric media is given by

$$\varepsilon(\vec{r}, t) = \begin{bmatrix} \varepsilon_x(\vec{r}, t) & 0 & 0 \\ 0 & \varepsilon_y(\vec{r}, t) & 0 \\ 0 & 0 & \varepsilon_z(\vec{r}, t) \end{bmatrix}. \tag{76}$$

In this case, (75) may be written in the form of three scalar cartesian equations as

$$D_x = \varepsilon_x(\vec{r}, t)E_x \tag{77}$$
$$D_y = \varepsilon_y(\vec{r}, t)E_y \tag{78}$$
$$D_z = \varepsilon_z(\vec{r}, t)E_z. \tag{79}$$

At first, we consider the discretization of (77)–(79) for field expansions using only scaling functions in space domain. Assuming that the field expansions of the electric field components are given by (6), the electric flux components have to be expanded in a consistent manner as shown below

$$\begin{aligned} D_x(\vec{r}, t) = &\sum_{k,l,m,n=-\infty}^{+\infty} {}_kD^{\phi x}_{l+1/2,m,n} h_k(t)\phi_{l+1/2}(x) \\ &\cdot \phi_m(y)\phi_n(z) \\ D_y(\vec{r}, t) = &\sum_{k,l,m,n=-\infty}^{+\infty} {}_kD^{\phi y}_{l,m+1/2,n} h_k(t)\phi_l(x) \\ &\cdot \phi_{m+1/2}(y)\phi_n(z) \\ D_z(\vec{r}, t) = &\sum_{k,l,m,n=-\infty}^{+\infty} {}_kD^{\phi z}_{l,m,n+1/2} h_k(t)\phi_l(x) \\ &\cdot \phi_m(y)\phi_{n+1/2}(z) \end{aligned} \tag{80}$$

where ${}_kD^{\phi\kappa}_{l,m,n}$ with $\kappa = x, y, z$ are the expansion coefficients for the field expansions in terms of scaling functions.

We insert the field expansions in (77)–(79) and sample the equations using pulse test functions with respect to time and scaling test functions with respect to space. Assuming

$$\varepsilon_\kappa(\vec{r}, t) = \varepsilon_\kappa(x)\varepsilon_\kappa(y)\varepsilon_\kappa(z)\varepsilon_\kappa(t) \tag{81}$$

and sampling e.g. (77) with $\phi_{l+1/2}(x)\phi_m(y)\phi_n(z)h_k(t)$ yields

$$\begin{aligned} {}_kD^{\phi x}_{l+1/2,m,n} = &\sum_{k',l',m',n'=-\infty}^{+\infty} \varepsilon^{\phi x}_{(x)l+1/2,l'+1/2}\varepsilon^{\phi x}_{(y)m,m'} \\ &\cdot \varepsilon^{\phi x}_{(z)n,n'}\varepsilon^{x}_{(t)k,\,k'k'} E^{\phi z}_{l'+1/2,m',n'} \end{aligned} \tag{82}$$

TABLE IV
THE COEFFICIENTS B_i AND C_i

i	B_i	C_i
0	1.96976160	
1	-0.67243039	2.89173391
2	0.26870415	-2.00521039
3	-0.11851986	0.54227884
4	0.05519138	-0.01207123
5	-0.02652026	0.14408849
6	0.01299809	-0.14591233
7	-0.00645742	0.00301822
8	0.00323979	0.02834407
9	-0.00163770	0.01914911
10	0.00083276	-0.02246183

where $\varepsilon^{\phi x}_{(\kappa)m,m'}$ and $\varepsilon^{x}_{(t)k,k'}$ are integrals given by

$$\varepsilon^{\phi x}_{(\kappa)m,m'} = \frac{1}{\Delta\kappa}\int \phi_m(\kappa)\varepsilon_x(\kappa)\phi_{m'}(\kappa)\,d\kappa \tag{83}$$

and

$$\varepsilon^{x}_{(t)k,k'} = \frac{1}{\Delta t}\int h_k(t)\varepsilon_x(t)h_{k'}(t)\,dt. \tag{84}$$

Defining the electric flux component vectors

$$|D_{\phi\kappa}\rangle = \sum_{k,l,m,n=-\infty}^{+\infty} {}_kD^{\phi\kappa}_{l,m,n}|k; l, m, n\rangle \tag{85}$$

as vectors in $\mathcal{H}_{m\otimes t}$, (82) may be represented by the operator equation

$$\boldsymbol{X}^\dagger_h|D_{\phi x}\rangle = \boldsymbol{X}^\dagger_h\boldsymbol{\varepsilon}_{\phi x}|E_{\phi x}\rangle. \tag{86}$$

The operator $\boldsymbol{\varepsilon}_{\phi x}$ is given in dyadic notation by

$$\begin{aligned} \boldsymbol{\varepsilon}_{\phi x} = &\sum_{k,l,m,n=-\infty}^{+\infty}\sum_{k',l',m',n'=-\infty}^{+\infty} |k; l, m, n\rangle\varepsilon^{\phi x}_{(x)l,l'} \\ &\cdot \varepsilon^{\phi x}_{(y)m,m'}\varepsilon^{\phi x}_{(z)n,n'}\varepsilon^{x}_{(t)k,k'}\langle k'; l', m', n'|. \end{aligned} \tag{87}$$

The operator equation (86) represents the general discretization for time- and space-dependent symmetric anisotropic dielectric media. Note that the integral with respect to time may also be evaluated in frequency domain allowing the modeling of frequency-dependent dielectric media described by $\varepsilon(\vec{r}, \omega)$.

For the evaluation of the integrals (83), we use a simple representation of the scaling function in terms of cubic spline functions [16]. The cubic spline Battle–Lemarie scaling function in space domain may be expressed as

$$\phi(x) = \sum_{i=-\infty}^{+\infty} B_i B(x - i) \tag{88}$$

where the cubic spline function $B(x)$ is defined as

$$B(x) = \begin{cases} \dfrac{2}{3} - x^2 + \dfrac{|x|^3}{2} & \text{for } |x| \le 1 \\ \dfrac{1}{6}(2 - |x|)^3 & \text{for } 1 < |x| \le 2 \\ 0 & \text{for } |x| > 2. \end{cases} \tag{89}$$

TABLE V
RESONANT FREQUENCIES FOR A CAVITY HALF FILLED WITH DIELECTRIC MATERIAL

Analytic values	S-MRTD scheme (mesh size 2 × 4 × 3)		Yee's FDTD scheme (mesh size 10 × 20 × 15)	
	Absolute values	Relative error	Absolute values	Relative error
18.627 MHz	18.715 MHz	0.472 %	18.615 MHz	-0.065 %
27.172 MHz	27.350 MHz	0.654 %	27.140 MHz	-0.119 %
29.375 MHz	29.580 MHz	0.699 %	29.215 MHz	-0.544 %
35.069 MHz	35.280 MHz	0.601 %	34.970 MHz	-0.283 %

Table IV gives some of the expansion coefficients B_i. Usually, the coefficients B_i for $i > 9$ will be negligible. The coefficients B_i for $i < 0$ are given by the symmetry relation $B_i = B_{-i}$.

Table V exhibits the results for the first four resonant frequencies of the cavity depicted in Fig. 15, where one half is filled with dielectric material with a relative permittivity of $\varepsilon_r = 64$ and the other half is filled with air. The cavity has the dimensions 1m × 2m × 1.5m. For the analysis using Yee's FDTD scheme, a mesh with $\Delta l = 0.1$m was used resulting in a total number of 3 000 grid points. Analyzing the cavity with the S-MRTD scheme, a mesh with $\Delta l = 0.5$m was chosen reducing the total number of grid points by a factor of 125. The time discretization interval $\Delta t = 0.9 \cdot 10^{-10} s$ was again identical for both schemes as well as for the Wy-MRTD scheme used later on. In comparison with Yee's FDTD scheme, the execution time for the analysis using the S-MRTD scheme was reduced by a factor of nine to ten. Modeling the cavity depicted in Fig. 15, the nonzero matrix elements of the permittivity tensor in cartesian components are given by

$$\varepsilon_\kappa(\vec{r}, t) = \varepsilon_\kappa(y). \tag{90}$$

For $\varepsilon_\kappa(y)$, considering the image principle and a periodic structure with respect to the y-coordinate, respectively, we use

$$\varepsilon_\kappa(y) = \begin{cases} 1 & \text{for } y_0(2N-1) < y < 2y_0N \\ 64 & \text{for } 2y_0N < y < y_0(2N+1) \end{cases} \tag{91}$$

with $N = -\infty, \cdots, -1, 0, 1, \cdots, \infty$. The cavity is centered at $y = 0$ and has the length y_0 with respect to the y-coordinate. The operator $\boldsymbol{\varepsilon}_{\phi x}$ reduces to

$$\boldsymbol{\varepsilon}_{\phi x} = \sum_{m,m'=-\infty}^{+\infty} |m\rangle \varepsilon^{\phi x}_{(y)m,m'} \langle m'|. \tag{92}$$

Now the operator equation (86) gives rise to a linear matrix equation which can be inverted before program execution. Note that the use of

$$\varepsilon_\kappa(y) = \begin{cases} 1 & \text{for } y < 0 \\ 64 & \text{for } y > 0 \end{cases} \tag{93}$$

simplifies the evaluation of the integral (83), however it provides only an approximation of the correct matrix equation, since the mesh is so small that some major matrix elements have to be neglected. Note that for larger meshes, the use of (93) yields results with good accuracy when a matrix of the size 7 × 7 and larger is used.

We consider the discretization of (77) for field expansions with scaling and wavelet functions in space domain. With respect to the cavity half-filled with dielectric material, one can only expect an improvement for the accuracy of the resonant frequencies by adding wavelets with respect to the y-coordinate: The field distribution of the modes are a product of the field distributions in x-, y- and z-direction. The spectral representations of the distributions in x- and z-direction contain only parts with low spectral frequencies. Thus the field expansions in terms of scaling functions allow a correct modeling of these distributions. The spectral representation of the field distribution in y-direction, however, does contain parts with high spectral frequencies due to the discontinuity at $y = 0$. Therefore, additional wavelets with respect to the y-coordinate have to be introduced to ensure a correct field representation.

Adding wavelets with respect to the y-coordinate, we expand the electric field components according to (47). Using similar field expansions for the electric flux components, we sample (77) with the functions $\phi_{l+1/2}(x), \phi_m(y), \phi_n(z)$ and $h_k(t)$ as well as with $\phi_{l+1/2}(x), \psi_{m+1/2}(y), \phi_n(z)$ and $h_k(t)$. Assuming a permittivity tensor according to (90), we obtain

$$\begin{aligned} {}_kD^{\phi x}_{l+1/2,m,n} = \sum_{m'=-\infty}^{+\infty} & (\varepsilon^{\phi x}_{(y)m,m'} \, {}_kE^{\phi z}_{l+1/2,m',n} \\ & + \varepsilon^{Ix}_{(y)m,m'+1/2} \, {}_kE^{\psi z}_{l+1/2,m'+1/2,n}) \end{aligned} \tag{94}$$

and

$$\begin{aligned} {}_kD^{\psi x}_{l+1/2,m+1/2,n} = \sum_{m'=-\infty}^{+\infty} & (\varepsilon^{Ix}_{(y)m',m+1/2} \, {}_kE^{\phi z}_{l+1/2,m',n} \\ & + \varepsilon^{\psi x}_{(y)m+1/2,m'+1/2} \, {}_kE^{\psi z}_{l+1/2,m'+1/2,n}) \end{aligned} \tag{95}$$

with the integrals

$$\varepsilon^{\psi x}_{(\kappa)m,m'} = \frac{1}{\Delta\kappa} \int \psi_m(\kappa) \varepsilon_x(\kappa) \psi_{m'}(\kappa) \, d\kappa \tag{96}$$

and

$$\varepsilon^{Ix}_{(\kappa)m,m'} = \frac{1}{\Delta\kappa} \int \phi_m(\kappa) \varepsilon_x(\kappa) \psi_{m'}(\kappa) \, d\kappa. \tag{97}$$

Introducing the vectors

$$|D_{\psi\kappa}\rangle = \sum_{k,l,m,n=-\infty}^{+\infty} {}_kD^{\psi\kappa}_{l,m,n} |k; l, m, n\rangle \tag{98}$$

TABLE VI
RESONANT FREQUENCIES FOR A CAVITY HALF-FILLED WITH DIELECTRIC MATERIAL

Analytic values	Wy-MRTD scheme (mesh size $2 \times 4 \times 3$)	
	Absolute values	Relative error
18.627 MHz	18.640 MHz	0.069 %
27.172 MHz	27.240 MHz	0.249 %
29.375 MHz	29.470 MHz	0.324 %
35.069 MHz	35.175 MHz	0.302 %

as well as the operators

$$\boldsymbol{\epsilon}_{\psi x} = \sum_{m,m'=-\infty}^{+\infty} |m\rangle \varepsilon^{\psi x}_{(y)m,m'} \langle m'| \tag{99}$$

and

$$\boldsymbol{\epsilon}_{Ix} = \sum_{m,m'=-\infty}^{+\infty} |m\rangle \varepsilon^{Ix}_{(y)m,m'} \langle m'|. \tag{100}$$

Equations (94) and (95) may be represented as

$$\boldsymbol{X}_h^\dagger |D_{\phi x}\rangle = \boldsymbol{X}_h^\dagger \boldsymbol{\epsilon}_{\phi x} |E_{\phi x}\rangle + \boldsymbol{X}_h^\dagger \boldsymbol{\epsilon}_{Ix} |E_{\psi x}\rangle \tag{101}$$

and

$$\boldsymbol{X}_h^\dagger \boldsymbol{Y}_h^\dagger |D_{\psi x}\rangle = \boldsymbol{X}_h^\dagger \boldsymbol{Y}_h^\dagger \boldsymbol{\epsilon}_{Ix} |E_{\phi x}\rangle + \boldsymbol{X}_h^\dagger \boldsymbol{Y}_h^\dagger \boldsymbol{\epsilon}_{\psi x} |E_{\psi x}\rangle. \tag{102}$$

A simple representation of the wavelet function in space domain in terms of cubic spline functions [16] allows an easy numerical evaluation of the integrals in (96) and (97). The cubic spline Battle–Lemarie wavelet function may be expressed as

$$\psi(x) = \sum_{i=-\infty}^{+\infty} C_i B(2x - i) \tag{103}$$

where some of the expansion coefficients C_i are given by Table IV. The coefficients C_i for $i < 1$ are given by the symmetry relation $C_i = C_{2-i}$.

The results for the resonant frequencies of the cavity with dielectric material using the Wy-MRTD scheme are shown in Table VI. In comparison to the results calculated by the S-MRTD scheme, the accuracy of the resonant frequencies is increased by a factor of two and more. On the other hand, there is an increase of the computer memory and execution time by a factor two and three. These results confirm that wavelets should be used locally in regions characterized by strong field variations in order to improve the accuracy of the field computation.

V. CONCLUSION

MRTD schemes based on orthonormal wavelet expansions have been derived and applied in the numerical analysis of simple microwave structures. The new schemes exhibit highly linear dispersion characteristics which result in the capability of providing excellent accuracy for a discretization close to the Nyquist sampling limit. Thus the minimum discretization for accurate MRTD results is close to two points per wavelength, whereas it is usually about ten points per wavelength for accurate FDTD results. This explains why the results for FDTD and MRTD exhibit about the same accuracy while using a MRTD mesh with five times less grid points per dimension. In comparison with Yee's FDTD scheme, our three-dimensional examples suggest computer savings of one order of magnitude with respect to execution time and two orders of magnitude with respect to the memory requirements.

It has been shown that the use of scaling functions in the method of moments leads to the S-MRTD scheme which allows a correct modeling of the electromagnetic fields provided their representation in spectral domain does not contain parts with high spectral frequencies. When the spectral domain representation of the fields does contain parts with high spectral frequencies, additional wavelet functions have to be considered. It has been demonstrated how to include wavelets in order to derive W-MRTD schemes based on both scaling and wavelets functions. However, these schemes are not efficient in the electromagnetic field modeling of homogeneous regions. Furthermore, the existence of spurious solutions leads to incorrect results and affects the accuracy of the field computation. Thus wavelets should be used locally for a variable mesh grading in regions characterized by strong field variations or field singularities in order to improve the accuracy of the field computation.

This conclusion is confirmed by the results for the dispersion characteristics of the S-MRTD scheme and the W-MRTD scheme with wavelets in one space dimension only. For a frequency interval up to the cutoff frequency of Yee's FDTD scheme, both MRTD schemes exhibit no dispersion error and no deviation from the linear dispersion relation, respectively. Thus for this large frequency interval, no improvement of the accuracy due to additional wavelets is possible. The improvements of the accuracy for larger frequencies are offset by an increase in computer resources and the existence of spurious solutions.

Furthermore, the complete theory for the treatment of symmetric anisotropic dielectric media has been presented. The application of the MRTD schemes based on orthonormal wavelet expansions does not allow for a localized modeling of the material properties as in Yee's FDTD scheme. This results in a higher complexity of the relationship between the electric flux and the electric field, but on the other hand, it allows the analysis of structures with arbitrary space-dependent permittivity.

REFERENCES

[1] K. S. Yee, "Numerical solution of initial boundary value problems involving Maxwell's equations in isotropic media," *IEEE Trans. Antennas Propagat*, vol. AP-14, no. 3, pp. 302–307, May 1966.
[2] J. C. Strikwerda, *Finite Difference Schemes And Partial Differential Equations*. Pacific Grove, CA: Wadsworth & Brooks, 1989.
[3] P. H. Aoyagi, J. F. Lee, and R. Mittra, "A hybrid yee algorithm/scalar-wave equation approach," *IEEE Trans. Microwave Theory Tech.*, vol. 41, no. 9, pp. 1593–1600, Sept. 1993.
[4] M. Mrozowski, "A hybrid PEE-FDTD algorithm for accelerated time domain analysis of electromagnetic waves in shielded structures," *IEEE Microwave Guided Wave Lett.*, vol. 4, no. 10, pp. 323–325, Oct. 1994.

[5] L. Lapidus and G. F. Pinder, *Numerical Solution Of Partial Differential Equations in Science and Engineering*. New York: Wiley, 1982, pp. 171–179.
[6] J. Fang, "Time domain finite difference computation for Maxwell's equations," Ph.D. dissertation, University of California at Berkeley, 1989, pp. 138–158.
[7] R. F. Harrington, *Field Computation by Moment Methods*. Malabar, FL: Krieger, 1982.
[8] M. Krumpholz and P. Russer, "Two-dimensional FDTD and TLM," *Int. J. Num. Modeling*, vol. 7, no. 2, pp. 141–153, Feb. 1993.
[9] ——, "A field theoretical derivation of TLM," *IEEE Trans. Microwave Theory Tech.*, vol. 42, no. 9, pp. 1660–1668, Sept. 1994.
[10] M. Krumpholz, C. Huber, and P. Russer, "A field theoretical comparison of FDTD and TLM," *IEEE Trans. Microwave Theory Tech.*, vol. 43, no. 8, pp. 1935–1950, Sept. 1995.
[11] S. G. Mallat, "A theory for multiresolution signal decomposition: The wavelet representation," *IEEE Trans. Pattern Anal. Machine Intell.*, vol. 11, pp. 674–693, July 1989.
[12] B. Jawerth and W. Sweldens, "An overview of wavelet based multiresolution analyses," *SIAM Rev.*, vol. 36, no. 3, pp. 377–412, Sept. 1994.
[13] G. Battle, "A block spin construction of ondelettes," *Comm. Math. Phys.*, vol. 110, pp. 601–615, 1987.
[14] P. G. Lemarie, "Ondelettes a localization exponentielle," *J. Math. Pures Appl.*, vol. 67, pp. 227–236, 1988.
[15] B. Z. Steinberg and Y. Leviatan, "On the use of wavelet expansions in the method of moments," *IEEE Trans. Antennas Propagat.*, vol. 41, no. 5, pp. 610–619, May 1993.
[16] K. Sabetfakhri and L .P. B. Katehi, "Analysis of integrated millimeter-wave and submillimeter-wave waveguides using orthonormal wavelet expansions," *IEEE Trans. Microwave Theory Tech.*, vol. 42, no. 12, pp. 2412–2422, Dec. 1994.
[17] I. Daubechies, "Ten lectures on wavelets," *SIAM Rev.*, Philadelphia, PA, 1992.
[18] P. Russer and M. Krumpholz, "The Hilbert space formulation of the TLM method," *Int. J. Numerical Modeling: Electronic Networks, Devices Fields*, vol. 6, no. 1, pp. 29–45, Feb. 1993.
[19] L. N. Trefethen, "Group velocity in finite difference schemes," *SIAM Rev.*, vol. 24, no. 2, Apr. 1982.
[20] D. R. Lynch and K. D. Paulsen, "Origin of vector parasites in numerical Maxwell solution," *IEEE Trans. Microwave Theory Tech.*, vol. 39, no. 3, pp. 383–394, Mar. 1991.
[21] J. Nielsen, "Spurious modes of the tlm condensed node formulation," *IEEE Microwave Guided Wave Lett.*, vol. 1, no. 8, pp. 201–203, Aug. 1991.
[22] M. Krumpholz and P. Russer, "On the dispersion in TLM and FDTD," *IEEE Trans. Microwave Theory Tech.*, vol. 42, no. 7, pp. 1275–1279, July 1994.

Michael Krumpholz, photograph and biography not available at the time of publication.

Linda P. B. Katehi (S'81–M'84–SM'89–F'95), for a photograph and biography, see p. 3 of the January 1996 issue of this TRANSACTIONS.